

Subproject F3.2

Materials for Lithium Batteries

Principle Investigators: Claus Feldmann

CFN-Financed Scientists: Silke Wolf (1/2 E13, 19 months)

Further Scientists: Silvia Diewald, Elin Hammarberg, Alexander Okrut, Michael Wolf

**Institut für Anorganische Chemie
Karlsruhe Institute of Technology (KIT)**

Materials for Lithium Batteries

Introduction and Summary

Future energy saving and energy storage will require a reduction of thermal loss processes, an increased overall efficiency as well as efficient storage devices. To this end, novel materials for application in high-power batteries such as lithium-ion batteries are required. With this CFN-project we focus on the synthesis of suitable metals and metal compounds via an ionic-liquid-based approach. These ionic liquids are known for their exceptional electrochemical and thermal stability. Moreover, they are frequently discussed as an inert electrolyte to be used in high-power batteries.

While exploring the potential of ionic liquids with regard to inorganic synthesis a manifold of new compounds was obtained. This includes the halogen-rich compounds $[\text{C}_4\text{MPyr}]_2[\text{Br}_{20}]$, $[\text{Pb}_2\text{I}_3(18\text{-crown-6})_2][\text{SnI}_5]$, $\text{CdI}_2(18\text{-crown-6})\cdot 2\text{I}_2$, $\text{Sn}_3\text{I}_8\cdot 2(18\text{-crown-6})$ as well as the chalcogen-rich compounds $[\text{Bi}_3\text{GaS}_5]_2[\text{Ga}_3\text{Cl}_{10}]_2[\text{GaCl}_4]_2\cdot \text{S}_8$, $[\text{Li}(12\text{-crown-4})_2]_2[\text{Sb}_2\text{Se}_{12}]$ and $[\text{Li}(12\text{-crown-4})_2]_4[\text{Te}_{12}](12\text{-crown-4})_2$. These compounds comprise novel compositions, structures and building units and prove that ionic liquids give access to a fascinating new type of chemistry. This statement is highlighted by $[\text{C}_4\text{MPyr}]_2[\text{Br}_{20}]$ representing the first three-dimensional infinite polybromide network and the halogen-richest compound known till now. The successful preparation of the above compounds with starting materials such as elemental halogens (e.g. Br_2) or elemental alkali metals (e.g. K), moreover, proves the potential of ionic liquids towards inorganic synthesis in terms of thermal/chemical stability.

In addition the high-power batteries, the synthesis of nanoscale elemental metals exhibiting uniform size and shape is also motivated by issues of fundamental research. Potential quantum size effects, superconducting properties and the use of reactive metals as a general platform to prepare metal compounds. With this CFN-subproject, the synthesis of uniform In^0 , Bi^0 and Cu^0 nanoparticles is established. Based on the synthesis of high-quality metal nanoparticles, on the one hand, its thermal sintering and melting was studied in situ. On the other hand, layer deposition and application in a light-sensitive electrochemical cell was tested.

Tests of the as-prepared compounds and metal nanoparticles regarding their potential in high-power batteries till now suffer from the fact that recruiting an expert in this field by the KIT is significantly delayed. Nevertheless, first studies were performed with nanoscale SnO_2 hollow spheres (stemming from our CFN project C1.4) by the CFN member H. Hahn. Moreover, the bromine-rich compound $[\text{C}_4\text{MPyr}]_2[\text{Br}_{20}]$ was successfully evaluated in a very first test of an lithium-bromine battery.

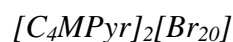
Metal nanoparticles, furthermore, turned out to be highly interesting for external partners and additional studies. This includes catalysis (Prof. G. Hutchings, University of Cardiff), $\text{Cu}(\text{Ga},\text{In})\text{Se}_2$ -based thin-film solar cells (Dr. E. Ahlswede, Zentrum für Solarenergie und Wasserstoffforschung, Stuttgart; Bayer company), seeds for gas-phase growth of nanowires (Prof. S. Schulz, Universität Essen), Plasmon-resonance induced emission (Prof. R. Schuster, KIT).

In the timeframe 2009-2010, subproject F3.2 has led to 9 publications, among which are 1 in *Angew. Chem.*, 1 in *Inorg. Chem.*, 1 in *J. Mater. Chem.*, 1 in *Chem. Mater.* and 1 patent.

1. Novel compounds via ionic liquid based synthesis

Ionic liquids (IL) are claimed to exhibit a range of exceptional properties. This includes a wide liquid range (−50 to +400 °C), an excellent thermal stability (up to 400 °C), a wide electrochemical window (−4 eV to +4 eV) and a low vapor pressure.¹ Nowadays, they can be composed of hundreds of different cations and anions which allows a specific fine-tuning of solvent properties (e.g. polarity, miscibility with other solvents, solubility of starting material, magnetic/luminescent properties).^{1,2} Based on the claimed exceptional features, ionic liquids can provide opportunities to chemical synthesis that differentiate significantly from conventional solvents – ranging from liquid NH₃ or SO₂, hydrothermal- and solvothermal synthesis to classical molten alkali metal halides.³ To date, ionic liquids have already gained considerable impact on organic synthesis,⁴ synthesis of nanomaterials,⁵ catalysis⁶ or development of inert electrolytes.⁷ Comparably high costs and a dramatical drop in quality when impurified with even low traces of water or impurities stemming from the synthesis or thermal decomposition of ionic liquids, on the other hand, can be regarded as current drawbacks.

Taking the exceptional properties ionic liquids for granted, the question may arise whether there is any benefit with concern to inorganic synthesis. Here, exploration has just begun. Some first results, such as a fascinating germanium clathrate or the chemistry of weakly coordinating anions (WCAs), suggest that ionic liquids indeed may give access to unique compounds and chemical reactions as compared to conventional solvents.⁸



As a part of our studies,⁹ we have explored the stability of ionic liquids towards strongly oxidizing halogens and in view of a formation of halogen-rich compounds. To this concern, the well-known polyhalides represent textbook chemistry and have been of particular interest for many years.¹⁰ To date the class of the polyhalides is dominated by the polyiodides exhibiting a generalized composition $[I_{n+m}]^{m-}$ (with $n(I^{\pm 0})$ and $m(I^{-1})$).¹¹ Their structural versatility can be considered as derived from the donor-acceptor interaction between the Lewis-bases I^- and $[I_3]^-$ and the Lewis-acid I_2 . These subunits act as “building blocks” and can be combined to largely expanded polyiodide anions such as $[I_{26}]^{3-}$ or $[I_{29}]^{3-}$.^{11b,12} Taking iodine contacts up to the sum of the doubled van-der-Waals radii (i.e. 420 pm) into account, a description as infinite one-, two- or three-dimensional networks is also often viable.¹³ More details regarding the huge number of different polyiodides were summarized in a review by Svenson and Kloo.¹⁰

Owing to the increasing reactivity and vapour pressure, knowledge on the lighter halogens and polyhalides is much more limited. In fact, polybromides are limited to $[Br_3]^-$, linear $[Br_4]^{2-}$, Z-shaped $[Br_8]^{2-}$ and ring-type $[Br_{10}]^{2-}$.¹⁴ Moreover, $[C_5H_6S_4Br]^+[(Br_3^-)(\frac{1}{2}Br_2)]$ and $[H_4Tppz^{4+}][(Br^-)_2(Br_4^{2-})]$ (Tppz: tetra(2-pyridyl)pyrazine) represent one-dimensional (1D) polybromide networks.¹⁵ And with $[TddBr_2]^{2+}[(Br^-)_2(Br_2)_3]$ ($[TddBr_2]^{2+}$: 4,5,9,10-tetrathiocino-[1,2-*b*:5,6-*b'*]-1,3,6,8-tetraethyl-diimidazolyl-2,7-dibromdithionium) a two-dimensional (2D) infinite polybromide network has been reported recently.¹⁶ Finally, $[Cl_3]^-$ and V-shaped $[(Cl_3)(Cl_2)]^-$ are known as polychlorides.¹⁷ And the existence of polyfluorides in addition to $[F_3]^-$ is still part of a controversial discussion.¹⁸

By synthesis in ionic liquids we were now successful in preparing $[C_4MPyr]_2[Br_{20}]$ (C_4MPyr : *N*-Butyl-*N*-methylpyrrolidinium) as the first three-dimensional (3D) polybromide network. According to the alternative description $[C_4MPyr]_2[Br^-]_2 \cdot 9(Br_2)$, the compound contains a remarkable amount of nine dibromine molecules, which is actually the highest amount of elemental bromine ever observed – except for the element itself. The title compound was gained with a yield of about 90 %

by dissolving elemental bromine in an equimolare mixture of the ionic liquids $[C_{10}MPyr]Br$ ($C_{10}MPyr$: *N*-Decyl-*N*-methylpyrrolidinium) and $[C_4MPyr]OTf$ (OTf : Triflate). Hereof, $[C_{10}MPyr]Br$ serves as a “bromide-donor”, whereas $[C_4MPyr]OTf$ acts as a “liquifier” to establish an eutectic mixture that is even liquid below room temperature and thereby allows growing suited single crystals. Note that these deep red, highly adhesive crystals melt at about +9 °C.

According to single-crystal structure analysis, $[C_4MPyr]_2[Br_{20}]$ crystallizes triclinic with space group $P\bar{1}$. The compound is constituted of a central bromide anion (Br_1) that is coordinated by six dibromine molecules (Figure 1). Note that all the central bromide anions are equivalent by inversion symmetry. Four of the Br_2 molecules serve as direct linkers between two central bromide anions (Br_1). The remaining two dibromine molecules (Br_3 – Br_4 , Br_5 – Br_6) also interlink the central bromide (Br_1), but in each case involving a longer distance (352 and 358 pm) to a second dibromine molecule (Br_5 – Br_6 , Br_7 – Br_8) that is positioned perpendicular to the first. This results in a connectivity via three (Br_1 – Br_5 – Br_6 ··· Br_7 – Br_1) and four (Br_1 – Br_3 – Br_4 ··· Br_6 – Br_5 – Br_1) bromine atoms (Figure 1). Beside the octahedral Br_2 -coordination around the central bromide, finally, an additional dibromine molecule (Br_{10} – Br_{10}) is attached to Br_8 (Figure 1).

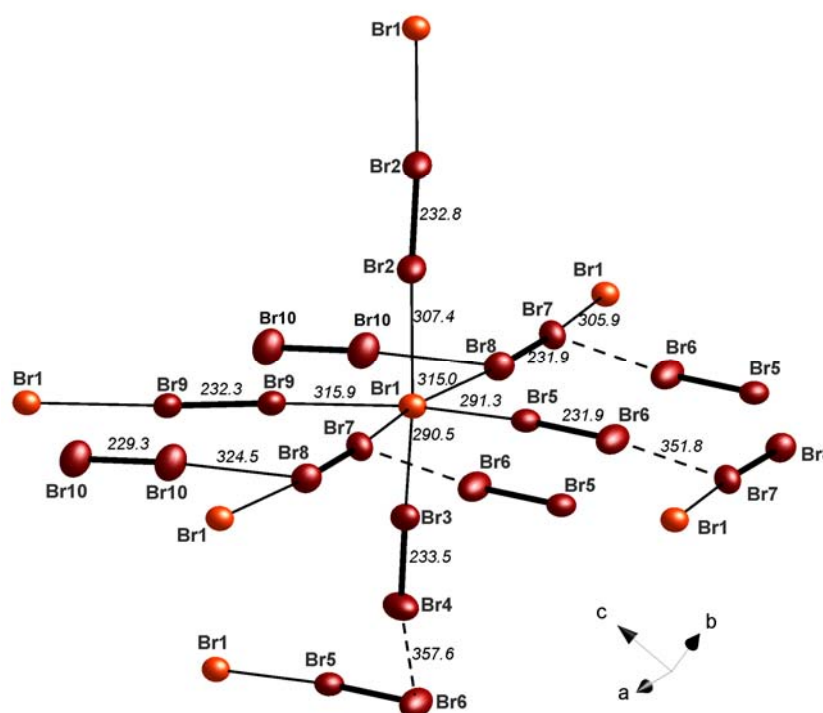


Figure 1. $[C_4MPyr]_2[Br_{20}]$ with the central bromide anion (Br_1 , light red) as the network node with coordinating dibromine molecules (Br_2 , dark red) as linkers (all Br–Br distances in pm; all thermal ellipsoids drawn with 50 % probability of finding).

With regard to the Br–Br distances, in sum, three different types are observed in $[C_4MPyr]_2[Br_{20}]$. The shortest distances (229–234 pm) represent the dibromine molecules and are slightly elongated in comparison to the element in the solid state (227 pm).³ Next, distances between dibromine molecules and the central bromide anion range from 291 to 316 pm. And finally even longer distances between 325 and 358 pm are observed between different dibromine molecules. These distances are still significantly below the doubled van-der-Waals radius of bromine (370 pm) (Figure 1, Table 1). A classification of $[C_4MPyr]_2[Br_{20}]$ in view of known polyhalides is not straightforward. Since the $Br^-(Br_2)$ distance for two dibromine molecules is about 5 % shorter (291 pm on average) as compared to the remaining four (311 pm on average), a

polymerized V-shaped (\simeq : 102 °) $[\text{Br}_5]^-$ anion might be extractable. Such $[\text{Br}_5]^-$ has not yet been reported in literature, too. On the other hand, the Br–Br distances are much closer to each other than the intramolecular/intermolecular distances observed for the polyiodides with common subunits $[\text{I}_{n+m}]^{m-}$ (with $n(\text{I}^{\pm 0})$ and $m(\text{I}^{-1})$).¹⁰ As a consequence, describing $[\text{C}_4\text{MPyr}]_2[\text{Br}_{20}]$ as a 3D-network ${}^3[(\text{Br}^-)_2(\text{Br}_2)_9]$ is much more meaningful. And this 3D-network is established without involving any other element than bromine. In addition to the unique 3D-network as well as the surprisingly high coordination of the central bromide by dibromine molecules, the title compound furthermore contains an even higher amount of the halogen (i.e. $\text{Br}^{\pm 0}:\text{Br}^{-1} = 18:2 = 9.00$) than the most iodine-rich polyhalide Fc_3I_{29} ($\text{I}^{\pm 0}:\text{I}^{-1} = 26:3 = 8.67$, Fc: Ferrocenium).^{11b}

Table 1. Br–Br distances (below the doubled van-der-Waals radius of 370 pm) of the title compound $[\text{C}_4\text{MPyr}]_2[\text{Br}_{20}]$ as compared to selected reference compounds.

Compound	Br–Br /pm (shortest distances)	Br–Br /pm (distances <370 pm)	Reference
$[\text{C}_4\text{MPyr}]_2[\text{Br}_{20}]^{2-}$	229 – 234	291 – 316 ($\text{Br}^- - \text{Br}_2$) 352 – 358 ($\text{Br}_2 - \text{Br}_2$)	
Br_2 (solid)	227	331 within layers (399 between layers)	[3]
$[\text{Q}^+][\text{Br}_3]^-$	246 – 265	–	[14b]
$[\text{Q}^+]_2[\text{Br}_8]^{2-}$	235 – 266	317 – 369	
$[\text{Dpfz}^+]_2[\text{Br}_{10}]^{2-}$	274 – 294	347 – 350	[14c]
$[\text{C}_5\text{H}_6\text{S}_4\text{Br}]^+[(\text{Br}_3^-)(\frac{1}{2}\text{Br}_2)]$	233 – 255	321 – 344	[15a]
$[\text{H}_4\text{Tppz}^{4+}][(\text{Br}^-)_2(\text{Br}_4^{2-})]$	242 – 297		[15b]
$[\text{TtddBr}_2]^{2+}[(\text{Br}^-)_2(\text{Br}_2)_3]$	236 – 241	304 – 370	[16]

(with Q^+ : quinuclidinium; Tppz: tetra(2-pyridyl)pyrazine; Dpfz: 1,5-Diphenylformazan; $[\text{TtddBr}_2]^{2+}$: 4,5,9,10-tetrathiocino-[1,2-*b*:5,6-*b'*]-1,3,6,8-tetraethyl-diimidazolyl-2,7-dibromdithionium)

Structurally the bromine network in $[\text{C}_4\text{MPyr}]_2[\text{Br}_{20}]$ can be formally rationalized based on distorted, corner-sharing $[(\text{Br}^-)(\text{Br}_2)_4(2\text{Br}_2)_2]^-$ octahedra (Figure 2). Distortion firstly originates from the different $\text{Br}^--(\text{Br}_2)$ distances. Secondly, it results from the fact that interlinking of the central bromide (Br_1) four-times involves a single dibromine and two-times two dibromine molecules. Note that the 9th dibromine molecule ($\text{Br}_{10}-\text{Br}_{10}$) is not bound to Br_1 (Figure 1). In sum, a ${}^3[(\text{Br}^-)_2(\text{Br}_2)_4(2\text{Br}_2)_2(\text{Br}_2)]$ network is obtained that includes $[\text{C}_4\text{MPyr}]^+$ cations as a kind of a template. Even the shortest C–H \cdots Br distances (292 pm, cf. Figure S1) are above of what is typically discussed as a bromine-hydrogen-bridge-bonding (240–290 pm).¹⁹ The long-ranging Madelung-type charge interaction between $[\text{C}_4\text{MPyr}]^+$ and the anionic network is nevertheless an important aspect with concern to the stability of the 3D-polybromide. Noteworthy, the structure of $[\text{C}_4\text{MPyr}]_2[\text{Br}_{20}]$ can also be described as a distorted CsCl-type of structure (Figure 2). This becomes obvious when only reckoning the central bromide anion (Br_1) and nitrogen as the center of the cation. With this perception, the Br^- serves as a network node that is interconnected by dibromine molecules as a linker.

Polybromides and bromine containing compounds, in general, are very rare to date. Typically, they consist of anionic bromidometallate-like building units and complexes such as $[\text{Cu}_2\text{Br}_6]^{2-}$, $[\text{Se}_2\text{Br}_{10}]^{2-}$, $[\text{Sb}_2\text{Br}_9]^{3-}$ or $[(\text{Me}_3\text{P})\text{AuBr}_3]$, which are most often bridged by one or two dibromine molecules.²⁰ To this concern, $[(\text{C}_4\text{H}_9)_4\text{N}]_2[\text{Pt}_2\text{Br}_{10}](\text{Br}_2)_7$ represents the compound with the highest content of bromine so far.²¹ Furthermore, $[\text{TtddBr}_2]^{2+}[(\text{Br}^-)_2(\text{Br}_2)_3]$ – as discussed in the introduction – represents a single example of an infinite polybromide 2D-network without any

additional element involved.¹⁶ Certain stabilization is here nevertheless observed to occur via interaction with sulfur and hydrogen atoms of the respective cation. As a result, $[\text{C}_4\text{MPyr}]_2[\text{Br}_{20}]$ – to the best of our knowledge – represents the first polybromide 3D-network that is exclusively established via interaction of bromine.

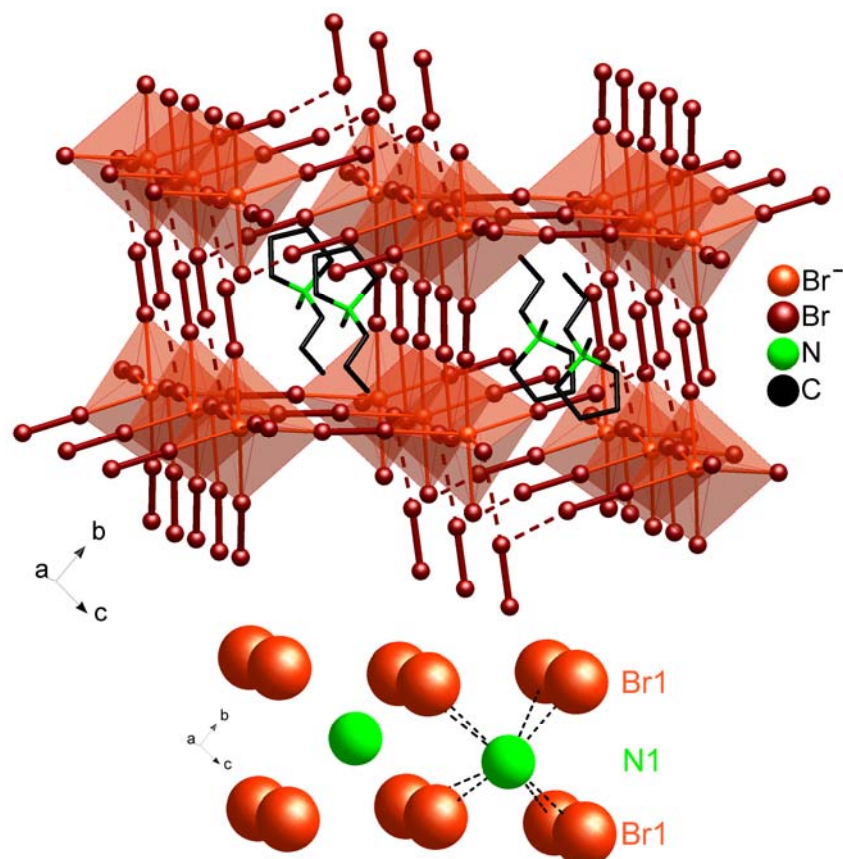


Figure 2. ${}^3_{\infty}[(\text{Br}^-)_2(\text{Br}_2)_4(2\text{Br}_2)_2(\text{Br}_2)]$ network in $[\text{C}_4\text{MPyr}]_2[\text{Br}_{20}]$ established by distorted corner-sharing $[(\text{Br}^-)(\text{Br}_2)_4(2\text{Br}_2)_2]^-$ octahedra (foreshadowed in light red) with the central bromide anion (Br1) as the network node that is interlinked by dibromine molecules (dark red with bold line). The $[\text{C}_4\text{MPyr}]^+$ cation serves as a templating agent in between of the polybromide 3D-network. Reckoning the central bromide anion as well as nitrogen as the center of the cation only, visualizes the correlation with a distorted CsCl-type structure (bottom).

In view of the unique features of $[\text{C}_4\text{MPyr}]_2[\text{Br}_{20}]$ a final question remains: What is special about the ionic liquid? Here, the stability of the eutectic mixture $[\text{C}_{10}\text{MPyr}]\text{Br}-[\text{C}_4\text{MPyr}]\text{OTf}$ towards oxidation is an obvious benefit. Even more important, however, is the low vapor pressure of dibromine in the applied eutectic ionic liquid. Qualitatively this can be rationalized just by looking at the gas phase above molten $[\text{C}_4\text{MPyr}]_2[\text{Br}_{20}]$ crystals at room temperature (Figure 3). In contrast to the pure element, the characteristic deep brown color of dibromine in the gas phase is missing. This finding closely correlates to the frequently reported low vapor pressure/high solubility of gases (e.g. H_2 , Ar, CO_2) in ionic liquids.^{1,2,22} Thermogravimetry allows to quantify the thermal decomposition in detail (Figure 3). Accordingly, $[\text{C}_4\text{MPyr}]_2[\text{Br}_{20}]$ decomposes with four steps: a) 60–190 °C (16.7 %); b) 190–290 °C (28.1 %); c) 290–420 °C (23.7 %); d) 420–550 °C (25.1 %). Although several reactions may certainly occur in parallel (e.g., evaporation of dibromine, radical bromination, evaporation of HBr , fragmentation of $[\text{C}_4\text{MPyr}]^+$) one can rationalize the decomposition as follows: a) -2Br_2 (exp. 17.0 %); b) -7HBr (exp. 30.0 %); c) $-2\text{C}_3\text{H}_6\text{Br}_2$ (exp.

21.4 %); d) $-\text{C}_6\text{H}_{10}\text{NBr}_3/\text{C}_6\text{H}_{11}\text{NBr}_2$ (exp. 31.5 %). The overall good agreement between experiment and expectation furthermore evidences the phase purity of the title compound.

The real surprise, however, is that no loss of dibromine occurred up to a temperature as high as $+60\text{ }^\circ\text{C}$. This low tendency to evaporate dibromine can be regarded as a crucial aspect to succeed with the preparation of bromine-rich compounds such as the polybromide 3D-network in $[\text{C}_4\text{MPyr}]_2[\text{Br}_{20}]$. To this regard, ionic liquids can open a doorway to novel halogen-rich compounds and a fascinating extension of the chemistry of the halogens. Moreover, ionic liquids may serve as a reservoir for bromine storage that – due to the low vapor pressure – allows a safer handling of the highly reactive halogens in chemical laboratories.

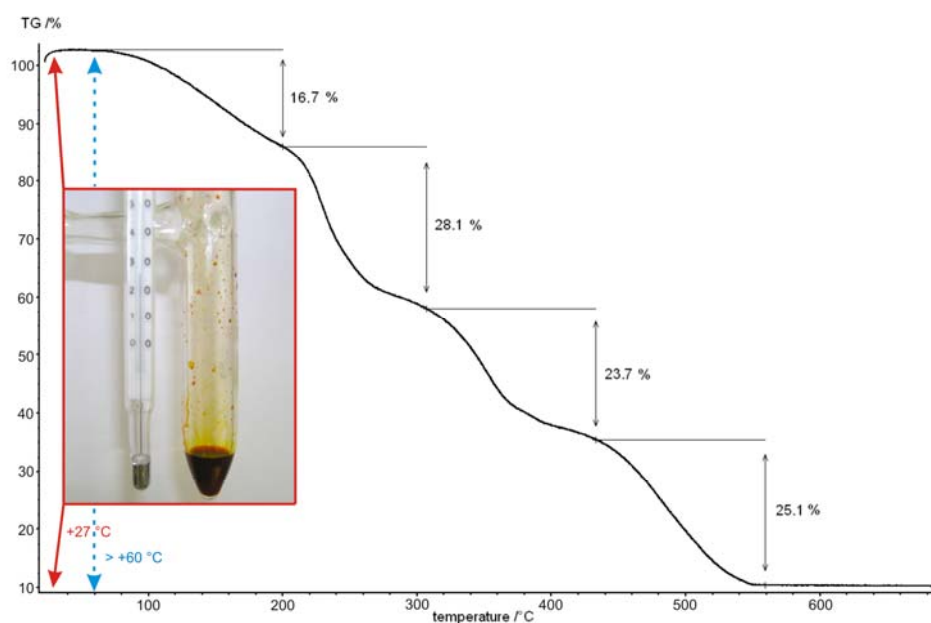


Figure 3. Foto of liquid $[\text{C}_4\text{MPyr}]_2[\text{Br}_{20}]$ at $+27\text{ }^\circ\text{C}$ and thermogravimetry of the pure title compound indicating a four-step weight loss between $+60\text{ }^\circ\text{C}$ and $+560\text{ }^\circ\text{C}$.



Via an Ionic-liquid-based synthesis, $[\text{Bi}_3\text{GaS}_5]_2[\text{Ga}_3\text{Cl}_{10}]_2[\text{GaCl}_4]_2 \cdot \text{S}_8$ is gained as a new compound that contains heterocubane-type $[\text{Bi}_3\text{GaS}_5]^{2+}$ cations, trimeric star-shaped $[\text{Ga}_3\text{Cl}_{10}]^-$ as well as single $[\text{GaCl}_4]^-$ anions and neutral crown-shaped S_8 rings (Figure 4). Hereof, $[\text{Bi}_3\text{GaS}_5]^{2+}$ represents the first cationic heterocubane in the system Bi–Ga–S. Moreover, $[\text{Ga}_3\text{Cl}_{10}]^-$ with three (GaCl_4) tetrahedra sharing a single central chlorine atom represents a new building unit with regard to the chemistry of the chlorometalates.

And finally one question remains in view of $[\text{Bi}_3\text{GaS}_5]_2[\text{Ga}_3\text{Cl}_{10}]_2[\text{GaCl}_4]_2 \cdot \text{S}_8$ – what is special about the synthesis in ionic liquids? This is, on the one hand, the inertness of the ionic liquid that does neither show a reaction or decomposition nor the coordinative properties of conventional polar solvents. Moreover, the ionic liquid guarantees for dissolution and proper diffusion of all reactants at mild conditions ($<150\text{ }^\circ\text{C}$). Such conditions obviously allow a preparation of complex, thermodynamically metastable compounds that as a pure compound decompose at temperatures similar to their synthesis in the ionic liquid.

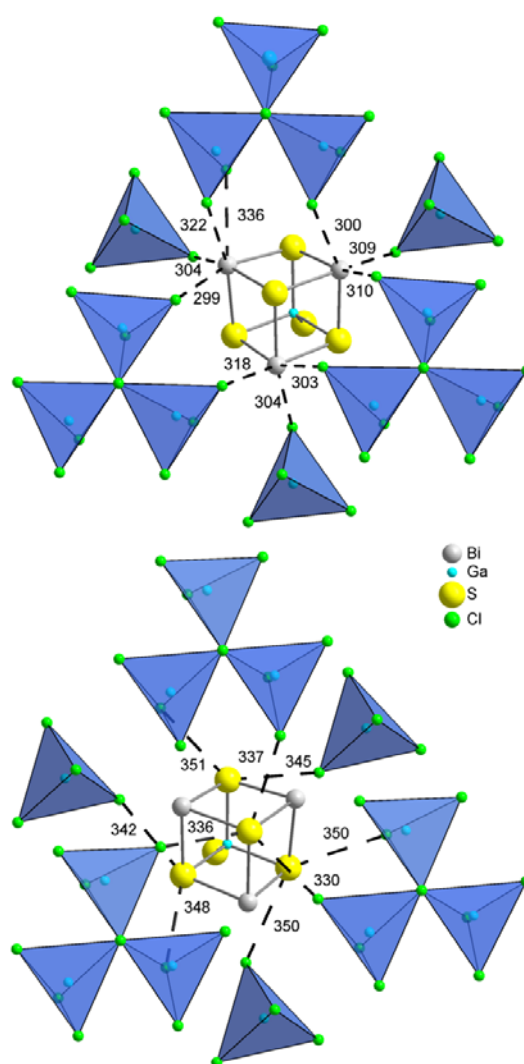
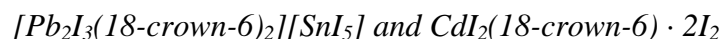


Figure 4. Coordination of the heterocubane cation $[\text{Bi}_3\text{GaS}_5]^{2+}$ with star-shaped $[\text{Ga}_3\text{Cl}_{10}]^-$ and monomeric $[\text{GaCl}_4]^-$ anions as well as Bi–Cl distances (top) and S–Cl distances (bottom) (all distances given in pm).



$[\text{Pb}_2\text{I}_3(18\text{-crown-6})_2][\text{SnI}_5]$ (**1**) and $\text{CdI}_2(18\text{-crown-6}) \cdot 2\text{I}_2$ (**2**) were prepared by reaction of PbI_2 , SnI_4 and 18-crown-6 as well as CdI_2 , I_2 and 18-crown-6 (Figure 5). All reactions were performed in the ionic liquid $[\text{NMe}(n\text{-Bu})_3][\text{N}(\text{Tf})_2]$, which serves as polar but aprotic liquid-phase providing a fast diffusion of the reactants at moderate temperatures (≤ 100 °C). **1** exhibits V-shaped $[\text{Pb}_2\text{I}_3(18\text{-crown-6})_2]^+$ cations and trigonal-bipyramidal $[\text{SnI}_5]^-$ anions. In $\text{CdI}_2(18\text{-crown-6}) \cdot 2\text{I}_2$ (**2**), the building unit $\text{CdI}_2(18\text{-crown-6})$ formally contains linear CdI_2 molecules that are interlinked by molecular iodine via long-ranging I–I contacts.

exhibits an endocyclical coordination of Sn^{2+} by the crown ether. Both constituents are linked via long-ranging I–I contacts to form an infinite network. Besides crystal structure analysis, the mixed valence state of tin is evidenced by ^{119}Sn -Mössbauer spectroscopy.

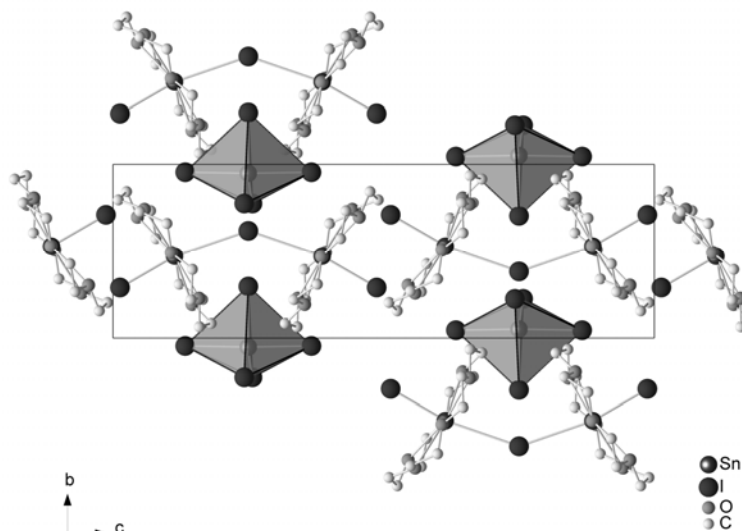


Figure 7. Unit cell of $\text{Sn}_3\text{I}_8 \cdot 2(18\text{-crown-6})$.

2. Metal nanoparticles

Indium nanoparticles

The synthesis of nanoscale elemental metals exhibiting uniform size and shape is motivated by issues of fundamental research as well as technical application.²³ Potential quantum size effects, superconducting properties and the use of reactive metals as a general platform to prepare metal compounds (i.e., InN , InP , InAs , In_2O_3 , In_2S_3) are points of interest.²⁴⁻²⁷ Heterogeneous catalysis (e.g. in organic synthesis), III-V semiconductors (e.g. for light emitting diodes) and optical materials (e.g. $\text{In}_2\text{O}_3:\text{Sn}$ as transparent conductive oxide) belong to those aspects of technological relevance.²⁴⁻²⁹ Right now, nanoscaled indium has been gained by gas-phase methods such as laser ablation,³⁰ evaporation techniques³¹ or thermal decomposition of organometallic compounds.³² Liquid-based synthesis has been performed applying polyol-type methods,³³ ionic liquids,³⁴ paraffin³⁵ or alkali metals³⁶ and alkalides/electrides³⁷ as strong reducing agents. Recently, octahedrally shaped and rod-like indium has been realized by NaBH_4 -initiated reduction in isopropanol.³⁸ Here, In^0 with 80-100 nm as lowest size has been realized in presence of polymer stabilizers such as polyvinylpyrrolidone. Altogether, advanced and expensive indium precursors as well as advanced synthesis techniques are quite often required in order to perform the reduction and to exclude moisture and air. Aiming at In^0 particles sized below 20 nm, the reactivity and moisture sensitivity will further increase.

In this study, the synthesis of uniform In^0 nanoparticles, 10-15 nm in diameter is assisted by a phase-transfer reaction. This two-step approach - including reduction in alcohol and phase transfer to alkanes - allows a straight-forward separation of In^0 nanoparticles from excess precursors as well as remaining salts, and guarantees a sufficient colloidal and chemical stabilization.

The two-step synthesis of In^0 nanoparticles was performed in detail as follows: at first, the indium precursor was dissolved in diethylene glycol (DEG) as the polar phase. This allows a usage of standard and low-cost indium salts (i.e., $\text{InCl}_3 \cdot 4\text{H}_2\text{O}$, $\text{In}_2(\text{SO}_4)_3 \cdot x\text{H}_2\text{O}$). Reduction of In^{3+} was performed thereafter by addition of NaBH_4 . As a second step, as-prepared indium nanoparticles

were separated from excess precursor and remaining salts by oleylamine-driven phase-transfer to non-polar dodecane or pentane. Reduction and phase transfer can be easily followed visually by the occurrence and location of dark brown indium (Fig. 8). Although so-called polyols (e.g., DEG, glycerol) are well-known for nanomaterials stabilization,³⁹⁻⁴² as-prepared In^0 in DEG is with limited stability regarding agglomeration and reoxidation. In fact, sedimentation and decolorization was observed within a day.

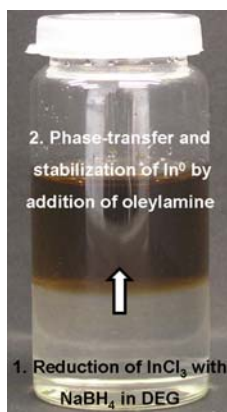


Figure 8. Scheme and photo of phase-transfer synthesis with In^0 nanoparticles located in the upper dodecane phase.

Subsequent to phase-transfer reaction, In^0 suspensions in dodecane exhibit a brownish, but transparent appearance and turn out to be stable within months (Fig. 9). According to dynamic light scattering (DLS), the mean hydrodynamic diameter of In^0 particles in dodecane amounts to 18 nm (Fig. 9). Thus, nanoscale particles with a narrow size distribution are formed. Size and absence of agglomerates are in accordance with the transparency and excellent stability of suspensions. Such suspensions can also be stored at ambient temperature in air. Neither a sedimentation of particles, nor a decolorization due to formation of colorless $\text{In}(\text{OH})_3$ or In_2O_3 was observed. Considering the reactivity of a nanoscaled, less-noble metal ($E_0(\text{In}) = -0.34 \text{ V}$)⁴³ the overall stability is quite high. Thus, beside colloidal stabilization the phase-transfer reaction also allows an efficient protection of In^0 against air- and moisture-driven oxidation. In fact, phase transfer driven by long-chained amines has been described previously, for instance in the case of CdSe-type quantum dots and Au nanoparticles.⁴⁴ The two-step sequence of metal reduction and particle nucleation in a polar phase followed by phase-transfer for separation and stabilization of less-noble metals, however has not been reported, yet.

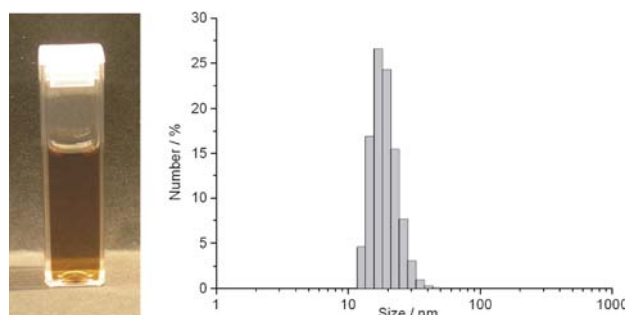


Figure 9. Photo and dynamic light scattering displaying the In^0 in dodecane after phase-transfer as well as the relevant particle size distribution.

Particle size and size distribution of as-prepared In^0 were further evaluated by scanning electron microscopy (SEM). Figure 10A shows as-prepared In^0 immediately after formation in DEG with uniform particles and very few agglomerates. In^0 nanoparticles are further displayed after

oleylamine-driven phase transfer to dodecane (Fig. 10B). In both cases the particle diameter amounts to 10-15 nm. In contrast to samples from DEG, those made from dodecane show a significant tendency to form agglomerates. This finding is in contradiction to DLS results as well as to the transparent appearance of suspensions. However, strong van-der-Waals interaction of the long-chained amine shell is to be expected and in accordance with the formation of particle clusters when drying the samples for electronmicroscopic characterization.⁴⁵

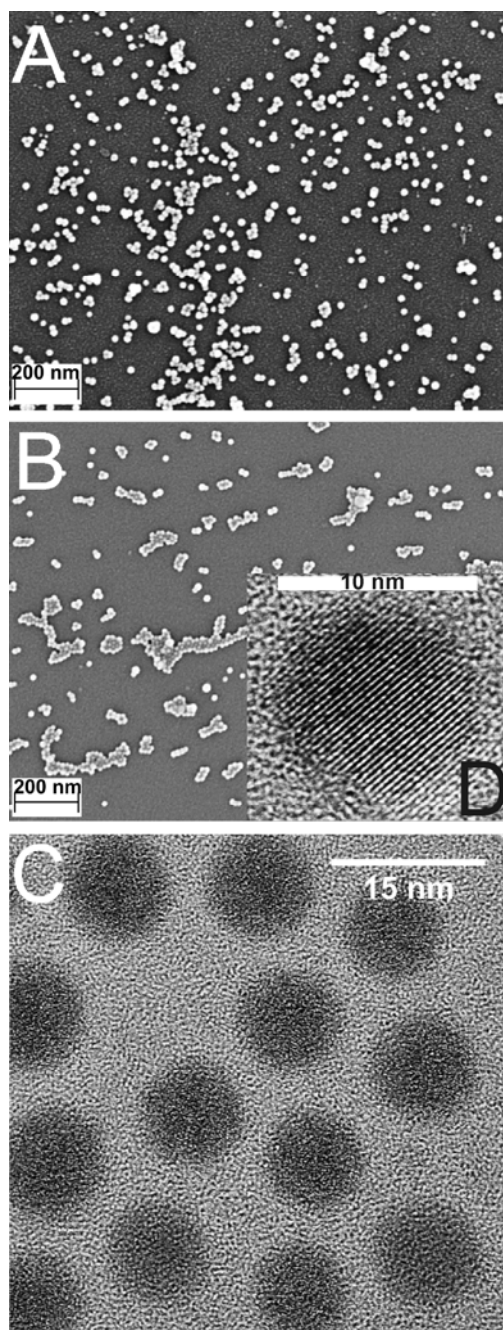


Figure 10. Electron microscopy of In^0 nanoparticles: A) SEM image of as-prepared In^0 in DEG phase; B) SEM and C) TEM image of as-prepared In^0 subsequent to phase-transfer in dodecane; D) HRTEM image with lattice fringes.

Characteristic TEM images exhibit spherical, non-agglomerated indium particles with a very uniform size and morphology (Fig. 10C). Distinct distances between individual particles again confirm the surface stabilization due to oleylamine. Obviously, the particles are non-agglomerated

and with particle diameters of 10-12 nm. Lattice fringes with d -values of 2.73(5) Å (Fig. 10D) are observed with a comparably weak contrast and confirm the presence of elemental indium (literature data: (100) with 2.72 Å).⁴⁶ In fact, the nanocrystals turn out to become non-crystalline under HRTEM conditions on a minutes time scale. Considering current densities up to 100 A/cm² at high magnification, such a finding is not surprising and has been reported previously.³² In addition to electron microscopy, crystallinity and composition of as-prepared In⁰ are further confirmed by X-ray powder diffraction patterns. Based on Scherrer's equation the crystallite size can be deduced to 15-20 nm.

Altogether, the phase-transfer reaction results in a straight-forward synthesis of uniform indium nanoparticles. Besides size and uniformity of these In⁰ particles, the usage of standard and low-cost indium salts, the facile separation from excess precursors and remaining salts and the sufficient colloidal and chemical stabilization can be denoted as special advantages of the synthetic approach. The two-step sequence of synthesis will be transferred to the formation of other metal nanoparticles next. Moreover, the resulting less-noble metals might be useful in order to establish less-noble metals as a general platform to nanoscale metal compounds such as oxides, sulfides, halogenides or nitrides.

Bismuth nanoparticles and its sintering and melting

In this study, submicron sized bismuth particles were used as a model system. The particles were gained via a polyol-mediated synthesis applying a microwave oven for sample preparation. Subsequent to synthesis the bismuth particles were transferred to a heater stage assembly that is mounted inside a scanning electron microscope. By sequential heating, the thermal behavior - namely sintering and melting - of as-prepared submicron-sized bismuth was observed *in situ*. Based on previous studies regarding the polyol-mediated synthesis of metals and oxides [47,48], the synthesis of elemental bismuth was carried out by dissolving Bi(NO₃) · 5 H₂O in glycerol. This solution was heated in 60 s to 240 °C via microwave irradiation. At temperatures of about 220 °C the solution almost instantaneously became black and turbid indicating the formation of solid bismuth. Finally, bismuth was separated via centrifugation and purified by repeated redispersion/centrifugation in/from isopropanol. Microwave irradiation indeed turned out to be superior to conventional resistant heating (e.g. with a heating mantle). This is due to the very fast heating rate (about 60 s) as well as due to the short overall time of heating. Both aspects result in a better control of nucleation and growth, which generates much more uniform particles in size and shape. Moreover, size distribution and degree of agglomeration are improved by microwave-induced heating. Similar results were found for nanoscale oxides [49-51]. Altogether the polyol-mediated synthesis of bismuth is quite facile since an additional reducing agent as well as an addition of base is not required.

Composition, purity and crystallinity of as-prepared bismuth particles are evidenced by X-ray powder diffraction. All Bragg peaks are in accordance to the reference. Scanning electron microscopy (SEM) was involved to get a closer look of morphology and size of as-prepared Bi. The particles turn out to be comparably uniform in size and shape. The average diameter was deduced by statistical evaluation of about 500 particles and resulted in 250 nm. The particles are muffled by a very thin, diffuse and weakly absorbing veil (< 2 nm), which is best visible at the interspaces between two particles. This veil can be attributed to remnant glycerol as a surface-bound colloidal stabilizer, its presence was investigated in detail in the case of oxide nanomaterials [50,52-54]. In addition to electron microscopy, the particle size distribution of the title compound is confirmed in suspension via dynamic light scattering (DLS). Here, an average hydrodynamic diameter of 263 nm is observed. The colloidal stability of the suspensions is ascribed to the viscosity of the solvent and to the polyol, which is adhered as a stabilizer on the particle surface [52,53].

With the availability of uniform submicron bismuth particles, its thermal behavior, sintering and melting can be studied. For *in situ* investigation inside a scanning electron microscope a heater stage assembly (Kammrath & Weiss, Dortmund) was applied. Most important are an aluminium plate with the Bi particles on its top side as well as a heater filament and a thermocouple (NiCrNi), which are located right below the sample. The aluminium plate is fixed with clips and can be exchanged quite easily. Aluminium was selected here for its low reactivity towards molten bismuth and the absence of intermetallic phases at temperatures below 600 °C [55]. Heater filament and thermocouple are thermally isolated from the base of the heater stage by a ceramic heat shield (α -Al₂O₃) in order to minimize heat transport to the housing of the electron microscope as a heat sink. Moreover, the base of the heater stage is cooled with water, pumped in through vacuum-tight passing from the outside of the microscope. With the heater stage assembly, in principle, a temperature range between room temperature and 800 °C is accessible. However, comparably strong vibration occurs above 500 °C, and therefore limits the resolution of SEM images. Practically, a temperature range up to 500 °C and particles with diameters of 100-500 nm or more turned out to be most useful.

To verify the thermal characteristics of the heater stage assembly, first of all, flakes (typically 1 mm times 1 mm in size) of different metals were placed on the aluminium plate as references. Thus, In, Sn, Bi, and Pb were heated and the melting point observed under *in situ* SEM conditions. The resulting values are compared to literature data. In general, the observed melting points turn out to be lower in comparison to literature data. Moreover, this deviation increases with temperature. Aiming at precise and reliable values, melting is normally measured under thermal equilibrium (e.g. calorimetric approach) [56]. To this concern, conditions of *in situ* SEM observation as conducted here, with vacuum on one side of the sample, the heater and a non-equilibrated housing as a heat sink on the other side, are definitely non-optimal by means of calorimetry. Taking the heat transport from the heater via the aluminium plate to the sample into account, a certain overheating is to be expected. Moreover, minor impurities as well as a lower melting due to the submicron-sized scale of the particles cannot be completely excluded. Altogether, the gap between as-observed melting of references and literature data is comparably low. Note that the following investigations do not aim at absolute melting temperatures, but at the behavior of a sample relative to a reference, applying the same experimental conditions for both.

For *in situ* observation as-prepared bismuth particles were deposited on the sample holder, at first. A typical situation is shown in Figure 11. Thereafter, the sample was heated slowly with a rate of 3 °Cmin⁻¹ to 200 °C. At 200 °C heating was proceeded with 1 °Cmin⁻¹ and interrupted in steps of 10 °C. At each step the sample was let to equilibrate thermally for 5 min in advance of taking a SEM image. Some typical images - always showing the identical area of the sample - are displayed in Figure 11. Surprisingly, not any significant change of particle size and shape is observed, even at temperatures of 400 °C. Only a certain shift of the heater stage and a certain variation in contrast occur. Both can be ascribed to increasing temperature and to charging effects. Sintering or melting, however, is not observed - even at a temperature about 140 °C above the melting point of bulk bismuth. This is most obvious in case of particles, which are located right beside to each other. This finding is also in contrast to bismuth flakes, which were used as a reference for temperature calibration.

The situation is even more surprising when enlarging the electron microscopic image (Fig. 12). Now it becomes obvious that all areas which have not been continuously exposed to the electron beam do show sintering and melting. Here, melting is observed - as expected - at temperatures (typically 250-280 °C) quite similar to the melting point of bulk Bi. As a consequence, submicron-sized bismuth particles altogether behave as expected. Just the most intensely scanned areas behave different. When cooled to room temperature, the differentiation of intensely scanned areas and almost non-scanned areas is stressed even further (Fig. 12). Obviously, the sample has been strongly affected by scanning. Taking a certain residue of glycerol as a stabilizer on the particle

surfaces into account, it can be assumed that this organic coating is partially decomposed under formation of amorphous carbon. In fact, examples showing such thermolysis or electron-beam induced pyrolysis of organic residues under exclusion of oxygen (e.g., in vacuum or under inert gas) are well documented [57-59]. Therefore, a rational assumption can be that the bismuth particles are covered by a certain carbon layer due to SEM investigation and electron-beam exposure. Since this low-absorbing layer is expected to be very thin (far below 1 nm) it can hardly be visualized via electron microscopy besides the strong absorbing bismuth. Aiming at a validation of this assumption, a controlled carbon coating of bismuth particles was applied next. If our hypothesis is valid this carbon coating should lead to a suppression of melting of all sample areas - scanned and non-scanned ones.

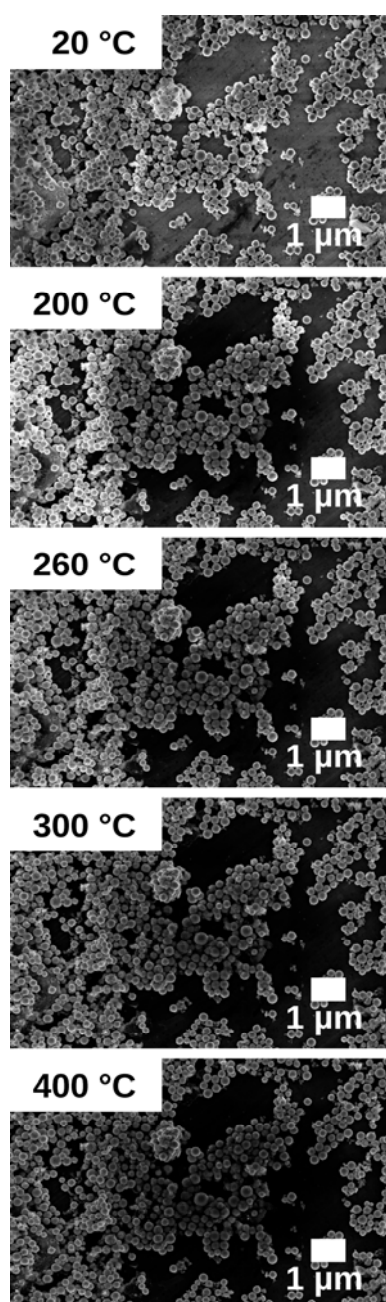


Figure 11. SEM images of bismuth particles at different sample temperatures.

To verify the hypothesis given above, the complete series of thermal experiments was repeated with bismuth particles sputtered with carbon black. Sputtering was performed via a standard carbon

coater. The resulting layer is clearly visible as a weakly absorbing film with a thickness of about 10 nm covering all particles. Again the sample was heated to 200 °C with a rate of 3 °Cmin⁻¹; collection of images started at 200 °C and was preceded in steps of 20 °C up to 480 °C. The results are shown in Figure 13 and Figure 14: first, an image at room temperature, second an image at 480 °C, and finally the sample after cooling to room temperature are pictured. Now, the bismuth particles do not show any morphological change or melting at all. The carbon layer is still clearly visible as a diffuse, weakly absorbing layer, which covers all bismuth particles. Altogether, the finding indeed confirms the hypothesis suggested above. Thus, one can conclude a certain carbon layer to efficiently suppress sintering and melting of submicron-sized bismuth particles, even at temperatures 200 °C above the melting point. Note that the aggregate state of bismuth inside the carbon shell remains an open question, yet.

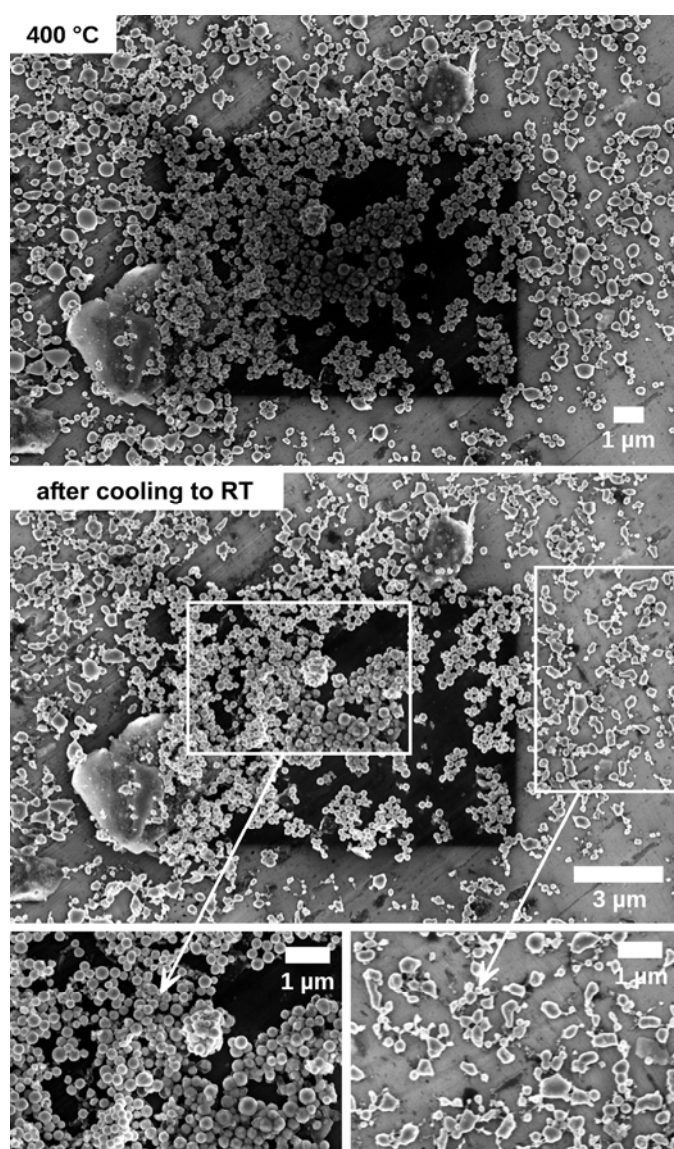


Figure 12. Large area SEM images of bismuth particles inside and outside continuously scanned areas at 400 °C, and after cooling to room temperature.

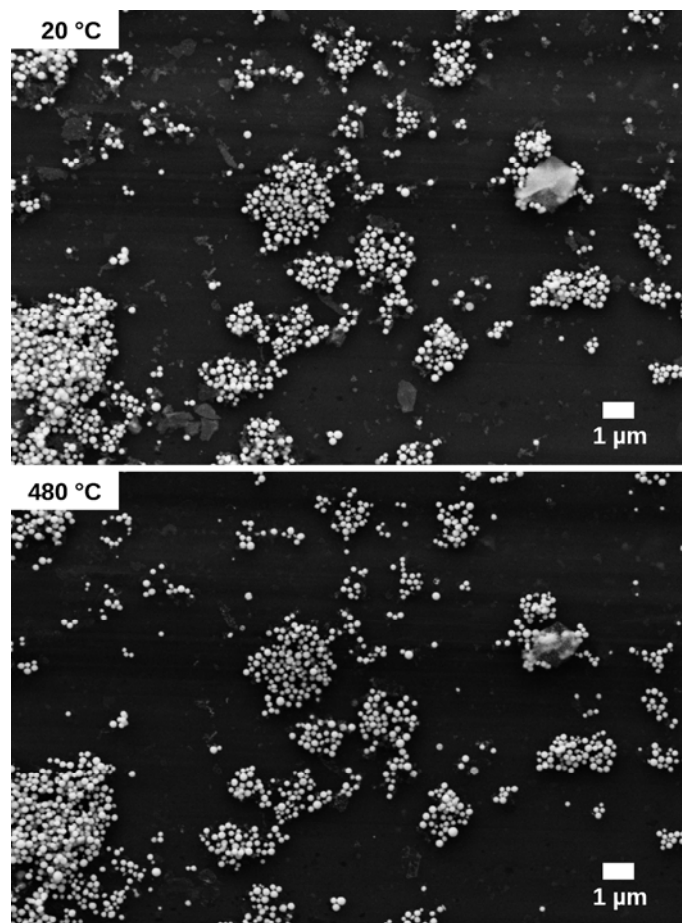


Figure 13. Large area SEM images of bismuth particles with controlled carbon coating at 20 °C and at 480 °C.

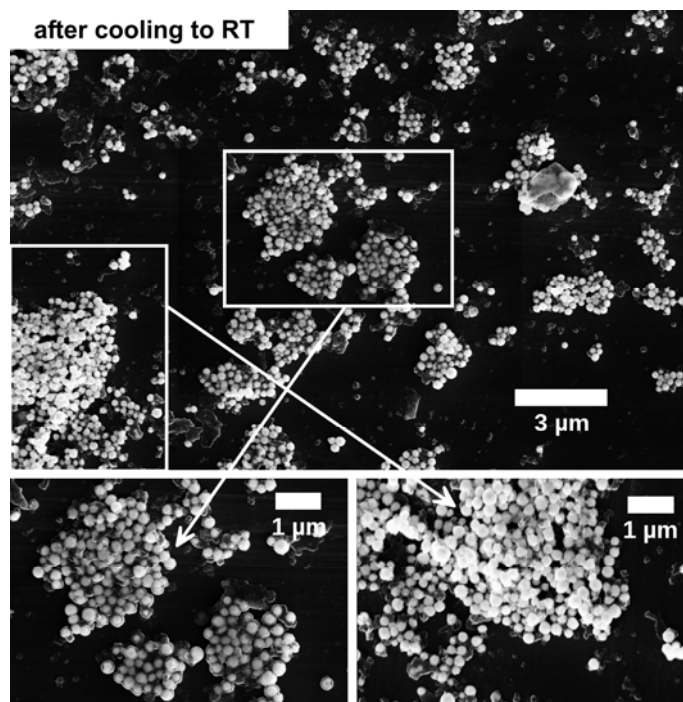


Figure 14. Large area SEM images of bismuth particles with controlled carbon coating after cooling to room temperature.

Bismuth nanoparticles and its photochromic behavior

A reversible photochromic effect was found for BiCl_3 -solutions in DEG. This finding is evidenced as a photocatalytical formation of Bi^0 nanoparticles, which is driven by the oxidation of DEG. Based on this reaction a simple electrochemical cell was established that allows detecting the intensity as well as the incidence of light. Especially the simplicity of the setup and the straightforwardness of its functions can be relevant for technical application and might lead to low-cost self-dimming foils, a facile optical marking of light-sensitive plastics or light-sensitive sensors, e.g., for one-way use.

To visualize the photochromic effect of BiCl_3 in DEG, the as-prepared solution was filled in a quartz cuvette and exposed to bright sunlight (Fig. 15). On a timescale of approximately 20 minutes the colorless and clear solution slowly changed, first to grayish, and finally to a deep black suspension. When brought into contact to air – just by shaking – the black suspension almost instantaneously cleared up color under dissolution of the solid particles (Fig. 15). Light exposure/blackening as well as re-oxidation/decolorization could be reversed several times. To understand the relevant chemical reactions and to validate its products, all the following experiments were conducted with BiCl_3 -solutions in DEG while involving different independent analytical tools.

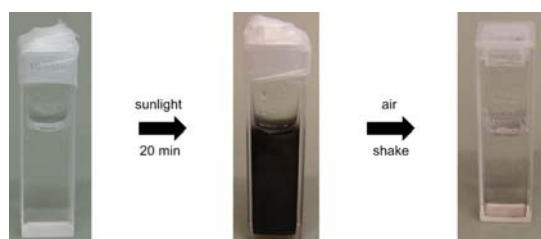


Figure 15. Reversible blackening and decolorization of a light-sensitive BiCl_3 -solution in DEG.

According to dynamic light scattering (DLS), light exposure and blackening are correlated to the formation of particles with a mean hydrodynamic diameter of 22 nm and a surprisingly uniform size distribution (15–30 nm). Electron microscopy confirms these results, again showing spherical and non-agglomerated particles, about 10–30 nm in diameter. Moreover, high-resolution TEM images of particle bundles indicate a high crystallinity of nanoscale bismuth. To this concern, the observed lattice fringes with a d-spacing of 320 pm evidence the presence of metallic bismuth ([012] with 328 pm).⁶⁰ Subsequent to re-oxidation and decolorization, bismuth was completely re-dissolved. Consequently, dynamic light scattering and electron microscopy do not show solid particles anymore. Note that a similar behavior – including blackening and decolorization – is observed with other alcohols, too (e.g., ethanol, glycerol). By comparison, the more viscous alcohols turned out to be preferable with regard to the colloidal stability of the formed nanoparticles. Since a polar alcohol in general is only a reasonable stabilizer of non-polar metal particles, agglomeration of particles is to be expected and observed the lower the viscosity of the liquid phase is and the longer the reaction proceeds. In the case of DEG, a certain agglomeration of bismuth nanoparticles occurred only after lengthened light exposure (> 1 h). These agglomerates started to precipitate and were therefore not available for re-oxidation by oxygen. The proceeding of the photochemical process, in principle, was not disturbed.

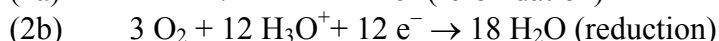
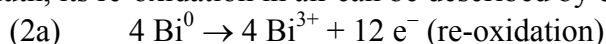
In addition to selected individual particles, the formation of metallic bismuth is also validated by X-ray powder diffraction after centrifugation of the black solid. Taking the formation of metallic bismuth as a matter of fact, the solvent DEG has to be considered as the reducing agent. To validate this assumption, the centrifugate – after separation of solid bismuth – was investigated via FT-IR spectroscopy. Herein, vibrations at $3600\text{--}3000\text{ cm}^{-1}$ ($\nu(\text{O-H})$), $2950\text{--}2850\text{ cm}^{-1}$ ($\nu(\text{C-H})$), 1200--

1000 cm^{-1} ($\nu(\text{C}-\text{O})$) as well as the finger-print area (1500–1200 cm^{-1}) can be attributed to DEG.⁶¹ Subsequent to light-induced bismuth formation, however, an additional vibration occurred at 1750–1550 cm^{-1} , which is assigned to $\nu(\text{C}=\text{O})$ and thereby confirms a partial oxidation of DEG under formation of the adjacent carbonic acid.

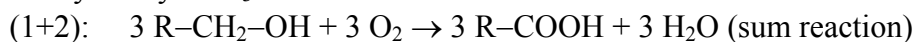
Considering these analytical results, the photochemical reaction can be concretized by equation (1a) and (1b):



According to previous studies a more complicated course of reaction and a radical mechanism has to be assumed. Most probably this includes an intermediate formation of Bi^{2+} radicals, which disproportionate thereafter.^{62,63} A radical mechanism is also well in accordance with a metal-compound-mediated oxidation of alcohols.^{64,65} Subsequent to the photochemical formation of bismuth, its re-oxidation in air can be described by equation (2a) and (2b):



As a sum reaction the alcohol is oxidized by oxygen to yield a carbonic acid and molar amounts of water (equation 1+2). By means of kinetics, this reaction proceeds at room temperature only if photocatalyzed by BiCl_3 .



The access to elemental metals via a polyol-mediated synthesis, in principle, is well established.^{67,68} As a general strategy, a metal salt as the starting material is dissolved in the polyol (i. e., a multidentate high-boiling alcohol such as glycerol, ethylene glycol, diethylene glycol) and reduced by this solvent at elevated temperatures. By increasing the temperature – and thereby the reductive strength of the polyol – up to 300 °C, noble metals (i. e., Pd, Pt, Ag, Au)⁶⁹⁻⁷³ and even less-noble metals (i. e., Co, Ni, In, Sn, Pb, Cd) can be gained.^{74,75} To this end, even the synthesis of Bi^0 is possible, but requires temperatures of at least 200 °C.⁷⁴⁻⁷⁶ A reduction at ambient temperature has been yet reported only in the case of noble metals (e. g., Ag, Au).⁷⁷ Naturally, re-oxidation just by air is not possible here. Although the polyol method in between represents a standard method of nanomaterials synthesis,⁷⁸ a reversible formation and re-dissolution of metal particles has not been described till now. Obviously, the complex and tender equilibrium of the electrochemical potential ($\text{Bi}^{3+} \leftrightarrow \text{Bi}^0$), the reductive force of DEG, the complex formation ($[\text{BiCl}_n]^{3-n} \leftrightarrow [\text{Bi}(\text{deg})_n]^{3+}$) as well as the activity of dissolved oxygen results in a unique situation.

To quantify the light-induced bismuth formation, UV-Vis spectroscopy was involved. First, the light-sensitive of BiCl_3 -solution in DEG was compared with the pure solvent as a reference. Indeed, an additional strong absorption is observed below 390 nm. Below this wavelength instantaneous blackening was observed; in contrast, no effect occurred at higher wavelength. Spectroscopic studies have already correlated the absorption to a $\text{Cl}^{-} \rightarrow \text{Bi}^{3+}$ ligand-to-metal charge-transfer (LMCT). The existence of non-dissociated Bi-Cl species in the presence of a chelating agent such as DEG, on the other hand, is surprising by first sight. Nevertheless, such species have been indeed identified spectroscopically as well as by single-crystal structure analysis.⁷⁹⁻⁸¹ As a next step, the complete photochromic effect was quantified by UV-Vis spectroscopy (Fig. 16). Hence, a decrease in transmission of about 30 % occurs upon light exposure almost instantaneously. By contact to air the suspension was decolorized recovering its original transmittance. In contrast, no decolorization was observed with nitrogen or argon as inert atmosphere. Altogether, the complete sequence of bismuth formation/blackening and re-oxidation/decolorization can be cycled many times since the solvent DEG acts as a quasi-infinite reservoir. Note that no similar effect was observed with BiBr_3 or BiI_3 . In contrast to BiCl_3 , the $\text{Br}^{-} \rightarrow \text{Bi}^{3+}$ - and $\text{I}^{-} \rightarrow \text{Bi}^{3+}$ -LMCT is located at increased wavelength (i. e., 450 nm and 650 nm), and therefore at lower energy, which is obviously not sufficient to initiate a reduction of Bi^{3+} .

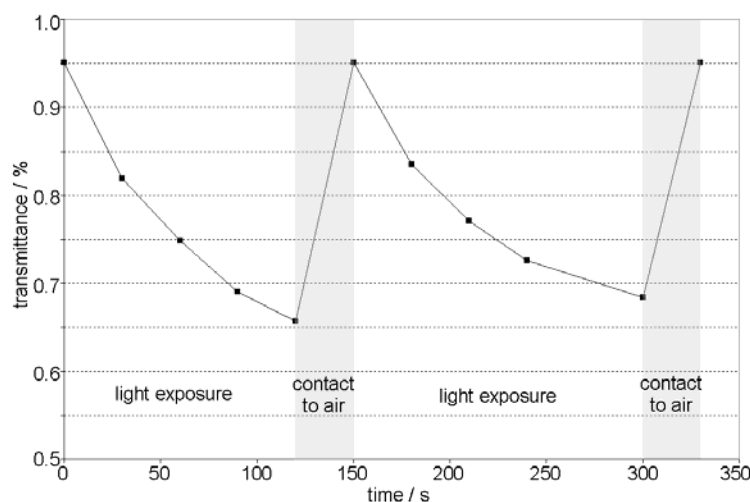


Figure 16. Reversible Bi^0 -formation/blackening and Bi^0 -re-oxidation/decolorization of a BiCl_3 -solution in DEG (white area: light exposure inside the UV-Vis spectrometer at 330 nm; grey area: contact to air by shaking the suspension).

Besides the photochromic effect, the underlying photocatalytic redox-process can also be used to establish a simple electrochemical cell. To this concern, the BiCl_3 -solution in DEG was filled between two ITO-sputtered glass plates (ITO: indium tin oxide), which were separated by a rubber gasket (Fig. 17). Moreover, the ITO electrodes were connected to a voltmeter and the resulting symmetrical cell was permanently kept in contact to air. Surprisingly, light exposure was indeed accompanied by a substantial electrochemical voltage. This finding can be ascribed to Bi^0 formation, which primarily occurs in the direction of the incoming light (Fig. 17). Thereafter, re-oxidation of Bi^0 – driven by oxygen dissolved in the DEG-solution – leads to a concentration gradient, with a low O_2 concentration at the side of the incoming light and a high O_2 concentration at the opposite side. As a consequence of these Bi^0 and O_2 concentration gradients, the cell becomes non-symmetric providing an electrochemical voltage. Hereof, the absolute value is directly correlated to the intensity of the incoming light; its sign indicates the direction of incidence.

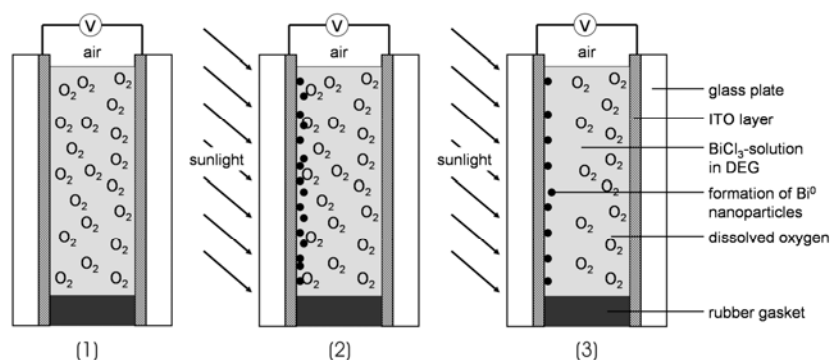


Figure 17. Scheme illustrating the construction of an electrochemical cell as well as the course of the photochemical reaction – in the order of (1)→(3).

In order to quantify the electrochemical voltage, measurements were conducted with monochromatized light (335 nm at variable slit width) of a high-power Xenon lamp (400 W). With a slit width of 3 nm a maximum voltage of ± 136 mV was obtained (Fig. 18). When increasing the intensity of light by adjusting a larger slit width (6 nm), the maximum voltage was increased to ± 407 mV. The incidence of light can be switched consecutively with response characteristics, again,

on a minute's timescale (Fig. 18). With ongoing switching a certain decrease of the maximum voltage is observed. This finding is ascribed to the consumption of dissolved oxygen and comparably slow oxygen dissolution from air into the DEG solution. Subsequent to a suitable regeneration (e. g. shaking of the DEG phase in air), the photochemical cell shows again its initial values. A further optimization of the electrochemical cell (e. g., layer thickness, concentration, viscosity) will further improve the turnover rate and the cycling stability. As prove of the concept the correlation between the electrochemical voltage and the intensity and incidence of light is nevertheless reliably validated. Considering the simplicity of this low-cost setup, the presented electrochemical cell might be a useful alternative to standard photochemical sensors based on, e. g., polyoxometallates or TiO₂-related composite materials.⁸²⁻⁸⁴

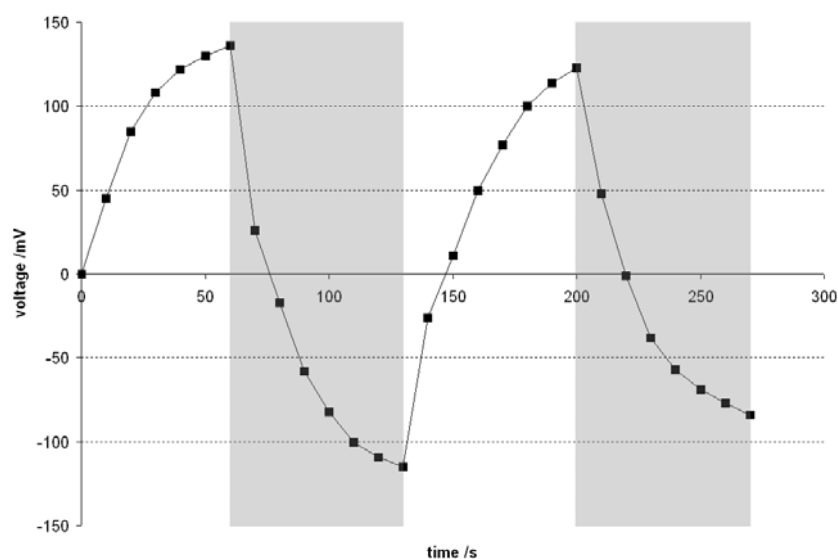


Figure 18. Voltage-versus-time diagram of the electrochemical cell with an alternating incidence of incoming sunlight (white and grey boxes indicate a changed incidence of light).

Copper nanoparticles and copper thin-films

This study focuses on an alternative strategy to thin-film copper electrodes, which includes Cu₂X(OH)₃ (X: Cl⁻, NO₃⁻) nanoparticle suspensions as precursor inks and boronhydride-driven reduction to copper at room temperature. Compounds with a pseudo-ternary composition Cu₂X(OH)₃ are known since decades and found as natural minerals (e.g., atacamite Cu₂Cl(OH)₃ in Chile).^{85,86} They play an important role in copper mining as well as for green colour pigments.⁸⁷ Surprisingly, knowledge on high-quality nanomaterials is very limited till now. Recently, platelet- and rod-type Cu₂Cl(OH)₃, 200 nm in size was gained via hydrothermal synthesis and studied with concern to hydrogen adsorption.⁸⁸⁻⁹⁰ Nanobelts of Cu₂Cl(OH)₃ with 50 nm in diameter and a length of several microns were described and decomposed to CuO with similar morphology.⁹¹ Moreover, Cu₂(NO₃)(OH)₃ was described with micron-sized particles.⁹² Based on our previous studies regarding the so-called polyol-mediated synthesis of nanomaterials,^{93,94} Cu₂Cl(OH)₃ and Cu₂(NO₃)(OH)₃ are here prepared using diethylene glycol diethyl ether (DEGEE) as a solvent and dispersant. Subsequent to synthesis, particle separation and washing, as-prepared Cu₂Cl(OH)₃ and Cu₂(NO₃)(OH)₃ are yielded as bright green to bluish-green powders.

According to the model given by LaMer and Dinegar⁹⁶ nucleation and growth of Cu₂Cl(OH)₃ and Cu₂(NO₃)(OH)₃ nanoparticles were performed based on homogeneous solutions of all reactants. In sum, our experimental approach is very comparable to the so-called polyol-mediated synthesis.⁹⁷

At this, nucleation and growth of nanoparticles is performed in high-boiling, multivalent alcohols (so-called “polyols”) such as glycol, diethylene glycol or glycerol. The polyol simultaneously serves as a solvent as well as a stabilizing agent. Since the synthesis can be performed at elevated temperatures (i.e. 100–350 °C), almost monodisperse and well-crystallized oxides are accessible quite often. Moreover, the polyol process is easy to perform and does neither require multisequential synthesis nor advanced experimental conditions or equipment. $\text{Cu}_2\text{Cl}(\text{OH})_3$ and $\text{Cu}_2(\text{NO}_3)(\text{OH})_3$ were prepared, in concrete, by dissolving CuCl_2 and $\text{Cu}(\text{NO}_3)_2 \cdot 2\text{H}_2\text{O}$ in diethylene glycol diethylether (DEGDEE). Nucleation of nanoparticles was initiated upon subsequent addition of NH_3 or NaHCO_3 , respectively. The surface of the growing particles is then instantaneously complexed by DEGDEE as a chelating agent. This complexation allows to effectively limit the particle growth and to suppress agglomeration. Finally, the nanoparticles were crystallized by heating to 100–150 °C. Note that – in contrast to the standard polyol process⁹⁷ – a high-boiling ether was used as the solvent instead of an alcohol. This is due to a significant solubility of $\text{Cu}_2\text{Cl}(\text{OH})_3$ and $\text{Cu}_2(\text{NO}_3)(\text{OH})_3$ in polyols such as diethylene glycol or glycerol. That would cause a poor control of particle nucleation and growth, and therefore lead to large, broadly sized particles.

To investigate size and morphology of $\text{Cu}_2\text{Cl}(\text{OH})_3$ and $\text{Cu}_2(\text{NO}_3)(\text{OH})_3$, dynamic light scattering (DLS) and scanning electron microscopy (SEM) were involved. At first, DLS analysis was performed subsequent to sample redispersion in ethanol (Fig. 19). These suspensions turned out to be colloidal stable within weeks. Moreover, a uniform size distribution with mean hydrodynamic diameters of 51 nm ($\text{Cu}_2\text{Cl}(\text{OH})_3$) and 37 nm ($\text{Cu}_2(\text{NO}_3)(\text{OH})_3$) is obtained. According to electron microscopy as-prepared nanoparticles are observed with spherical ($\text{Cu}_2\text{Cl}(\text{OH})_3$) to platelet-type ($\text{Cu}_2(\text{NO}_3)(\text{OH})_3$) shape and a low degree of agglomeration (Fig. 19). While the spherical morphology of $\text{Cu}_2\text{Cl}(\text{OH})_3$ is a direct consequence of isotropic growth according to LaMer-Dinegar model, the formation of ($\text{Cu}_2(\text{NO}_3)(\text{OH})_3$) platelets can be rationalized based on the underlying layer-type crystal structure of the bulk compound.⁹⁸ With average diameters of 44 nm ($\text{Cu}_2\text{Cl}(\text{OH})_3$) and 35 nm ($\text{Cu}_2(\text{NO}_3)(\text{OH})_3$) statistical evaluation based on at least 100 particles is in accordance to DLS analysis. Altogether, both methods confirm the presence of nanoscaled compounds and the absence of agglomerates.

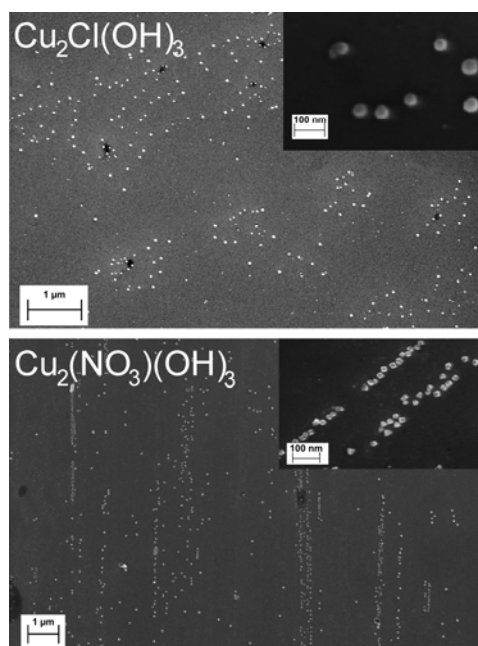


Figure 19: SEM images of as-prepared $\text{Cu}_2\text{Cl}(\text{OH})_3$ and $\text{Cu}_2(\text{NO}_3)(\text{OH})_3$ nanoparticles.

X-ray powder diffraction validates crystallinity, composition and purity of $\text{Cu}_2\text{Cl}(\text{OH})_3$ and $\text{Cu}_2(\text{NO}_3)(\text{OH})_3$. Thus, $\text{Cu}_2\text{Cl}(\text{OH})_3$ is obtained with the Atacamite modification, $\text{Cu}_2(\text{NO}_3)(\text{OH})_3$ with the Rouaite modification. Both modifications are known as the thermodynamically stable ones in the phase system at ambient conditions.⁹⁸ Moreover, infrared (FT-IR) and optical (UV-Vis) spectroscopy were conducted for materials characterisation. FT-IR spectra in both cases are dominated by $\nu(\text{OH}^-)$ ($3600\text{--}3300\text{ cm}^{-1}$). In the case of $\text{Cu}_2(\text{NO}_3)(\text{OH})_3$, furthermore, $\nu(\text{NO}_3^-)$ ($1500\text{--}1300\text{ cm}^{-1}$), $\gamma(\text{NO}_3^-)$ ($840\text{--}820\text{ cm}^{-1}$) and $\delta(\text{NO}_3^-)$ ($730\text{--}710\text{ cm}^{-1}$) are observed with strong intensity. The sharpness and splitting of vibrations is in accordance with a reduced site symmetry of the anions inside the crystalline host lattice.⁹⁹ Additional vibrations with comparably weak intensity can be related to H_2O ($\delta(\text{OH}_2)$: $1650\text{--}1600\text{ cm}^{-1}$) adhered on the particle surfaces as well as to lattice vibrations ($<900\text{ cm}^{-1}$). Note that the dispersant DEGDEE is not observed. Powder samples of $\text{Cu}_2\text{Cl}(\text{OH})_3$ and $\text{Cu}_2(\text{NO}_3)(\text{OH})_3$ exhibit a bluish-green to bright green colour that is quantified by UV-Vis spectra. Here, broad absorptions starting at about 380 nm and reaching up to 650 nm with its maxima at 505 nm and 503 nm are observed. In both these cases, the colour is ascribed to the $\text{O}^{2-} \rightarrow \text{Cu}^{2+}$ charge-transfer interaction, which is well-known for copper hydroxide based colour pigments.

Thermogravimetry (TG) was performed for thermal characterisation. Here, decomposition of $\text{Cu}_2\text{Cl}(\text{OH})_3$ is observed with 18.4 wt-% (2.9 mg) weight-loss below 300 °C, followed by 8.9 wt-% (1.4 mg) up to 600 °C. This finding is the sum of a first dissociation of HCl (expected: 17.1 wt-%) followed by H_2O (expected 8.4 wt-%) as a second step. Only a single very sharp decomposition step is observed for $\text{Cu}_2(\text{NO}_3)(\text{OH})_3$. Hence, 6.9 mg (33.7 %) weight loss occurs between 200 and 240 °C, which is in accordance with a contemporaneous dissociation of NO, NO_2 and H_2O (expected: 33.8 wt-%). The significantly lower temperature of decomposition of $\text{Cu}_2(\text{NO}_3)(\text{OH})_3$ is well in accordance with the low thermal stability of metal nitrates, in general.¹⁰⁰ Note finally that the TG-remnant – according to X-ray powder diffraction pattern – was identified as CuO in both cases.

In addition to thermal decomposition potential reduction of nanoscale $\text{Cu}_2\text{Cl}(\text{OH})_3$ and $\text{Cu}_2(\text{NO}_3)(\text{OH})_3$ to form copper metal was studied. Thus, powders of both compounds were reacted with a solution of 10 mol-% NaBH_4 in water. Room temperature reduction occurs instantaneously as indicated by a colour change from green to golden brown. X-ray powder diffraction of the dried solid remnant evidences the generation of metallic copper with minor amounts of Cu_2O as well as the complete vanishing of all starting materials. Based on these findings, deposition and printing of copper thin-films upon reduction of as-prepared $\text{Cu}_2\text{Cl}(\text{OH})_3$ and $\text{Cu}_2(\text{NO}_3)(\text{OH})_3$ nanoparticles was evaluated.

To study the layer structure and particle morphology, $\text{Cu}_2\text{Cl}(\text{OH})_3$ and $\text{Cu}_2(\text{NO}_3)(\text{OH})_3$ suspended with 10 wt-% in ethanol were first deposited on silicon wafers. Subsequent to drying in air, a coated Si-waver was dipped into the boronhydride solution. The deposited structures – prior and subsequent to reduction – are displayed in Figure 20. SEM images show a comparably dense layer of as-prepared $\text{Cu}_2\text{Cl}(\text{OH})_3$ nanoparticles. After reduction to copper metal, the particles exhibit a more plate-like morphology with a layer that is still dense. Based on these morphological studies, as-prepared $\text{Cu}_2\text{Cl}(\text{OH})_3$ and $\text{Cu}_2(\text{NO}_3)(\text{OH})_3$ nanoparticles were spin-coated on glass plates, too. These layers look identical to the above discussed layers on silicon. Electron microscopic characterisation of these layers, however, only allows images at low magnification due to significant charging on insulating glass plates, so that individual nanoparticles can not be resolved. Albeit layers on glass are less suitable for morphological characterisation, they are ideal for investigating the electrical properties. Consequently, the copper thin-films on glass – subsequent to NaBH_4 -driven reduction of $\text{Cu}_2\text{Cl}(\text{OH})_3$ and $\text{Cu}_2(\text{NO}_3)(\text{OH})_3$ and drying – were examined via four-point probing. As a result, sheet resistance of 3–10 Ω_{\square} were measured. Similar values were also found for thin-films spin-coated on plastic substrates. Taking the thickness of the deposited layers into account (approximately 2 μm), the specific resistivity was calculated to

$1.3\text{--}4.3 \cdot 10^{-3} \Omega\text{cm}$. These values match very well to the resistivity of bulk copper ($1.7 \cdot 10^{-3} \Omega\text{cm}$). Independent from the use of $\text{Cu}_2\text{Cl}(\text{OH})_3$ or $\text{Cu}_2(\text{NO}_3)(\text{OH})_3$ the deposited layers do not show a significant difference in terms of layer morphology or conductivity. Right now an initial contact of copper particles even in a porous layer turned out to be most essential. As a result, the conductivity is observed with values as given above or – if layer deposition is insufficient – with almost no conductivity at all.

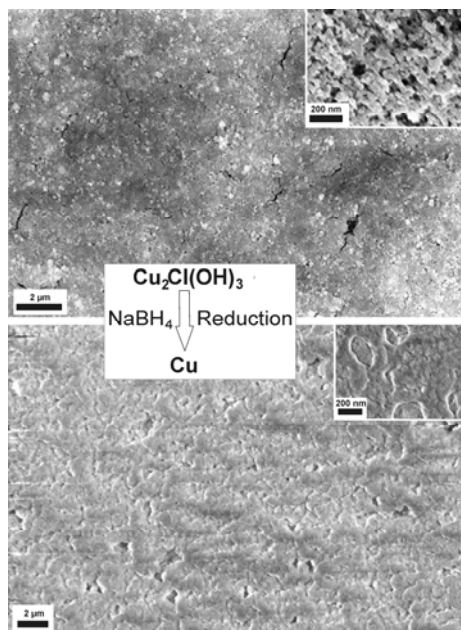


Figure 20: SEM images of $\text{Cu}_2\text{Cl}(\text{OH})_3$ nanoparticles printed on a silicon wafer prior as well as subsequent to NaBH_4 -initiated reduction to copper metal.

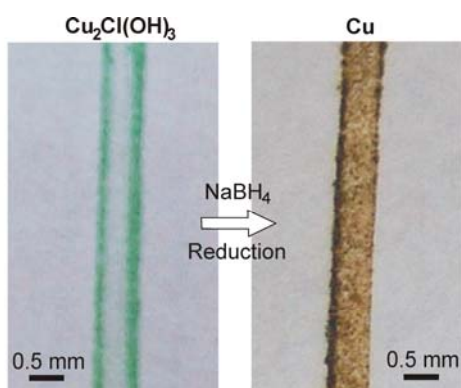


Figure 21: Photo of $\text{Cu}_2\text{Cl}(\text{OH})_3$ nanoparticles printed on paper, prior as well as subsequent to NaBH_4 -initiated reduction to copper metal.

Finally, as-prepared $\text{Cu}_2\text{Cl}(\text{OH})_3$ and $\text{Cu}_2(\text{NO}_3)(\text{OH})_3$ nanoparticles were printed on paper. As a proof of the concept, a rubber stamp was applied for printing on lab scale. To obtain a suitable “ink”, the nanoparticles were again resuspended in ethanol with solid contents of 10 wt-%. The printed structures were then dried, reduced by dip-contact to NaBH_4 solution, and once more dried. On paper the colour change from green to golden brown is clearly visible and indicates the reduction from $\text{Cu}_2\text{Cl}(\text{OH})_3$ and $\text{Cu}_2(\text{NO}_3)(\text{OH})_3$ to elemental copper (Fig. 21). Here, four-point probing results in sheet resistance of $4\text{--}5 \text{ k}\Omega_{\square}$. Due to the highly porous structure of paper, the thickness of the copper layer is less defined as compared to layers on silicon or glass. Therefore, we do not calculate a specific resistance here. Note that all printing experiments were performed without any

optimisation of those parameters that are relevant for real technical inks and its printing (e.g., viscosity, solids content, type of solvent, substrate pre-conditioning). Based on this proof of concept significantly improved layers (e.g. with concern to homogeneity and density), and thereby increased conductivities are to be expected while applying professional printing technologies.^{101,102} A further cost advantage may arise by the use of its formulations – as ink and paste – in high-quality printing techniques for the mask-less production of structured conductive electrodes.

References

- own work with complete titles -

- [1] a) P. Wasserscheid, T. Welton (Eds.), *Ionic Liquids in Synthesis*, Wiley-VCH, Weinheim 2008. b) R. Giernoth, *Angew. Chem.* **2010**, *122*, 2896–2300; *Angew. Chem. Int. Ed.* **2010**, *49*, 2834–2839.
- [2] a) N. Prondzinski, J. Cybinska, A. V. Mudring, *Chem. Commun.* **2010**, *46*, 4393–4395. b) E. Boros, M. J. Earle, M. A. Gilea, A. Metlen, A. V. Mudring, F. Rieger, A. J. Robertson, K. R. Seddon, A. A. Tomaszowska, L. Trusov, J. S. Vyle, *Chem. Commun.* **2010**, *46*, 716–718. c)
- [3] a) A. F. Hollemann, N. Wiberg, *Lehrbuch der Anorganischen Chemie*, de Gruyter, Berlin 2007. b) D. Shriver, P. Atkins, *Inorganic Chemistry*, Oxford Textbooks, London 2006.
- [4] a) Y. Liu, S. S. Wang, W. Liu, Q. X. Wan, H. H. Wu, G. H. Gao, *Current Org. Chem.* **2009**, *13*, 1322–1346. b) J. Dupont, R. F. de Souza, P. A. Z. Suarez, *Chem. Rev.* **2002**, *102*, 3667–3692.
- [5] M. Antonietti, D. Kuang, B. Smarsly, Y. Zhou, *Angew. Chem.* **2004**, *116*, 5096–5100; *Angew. Chem. Int. Ed.* **2004**, *43*, 4988–4992.
- [6] a) B. Ni, A. D. Headley, *Chem. Europ. J.* **2010**, *16*, 4426–4436. b) T. Jiang, B. Han, *Current Org. Chem.* **2009**, *13*, 1278–1299.
- [7] a) M. Armand, F. Endres, D. R. MacFarlane, H. Ohno, B. Scrosati, *Nature Mater.* **2009**, *8*, 621–629. b) M. Gorlov, L. Kloo, *Dalton Trans.* **2008**, 2655–2666.
- [8] a) A. M. Guloy, R. Ramlau, Z. Tang, W. Schnelle, M. Baitinger, Y. Grin, *Nature* **2006**, *443*, 320–323. b) J. M. Slattery, C. Daguinet, P. J. Dyson, T. J. S. Schubert, I. Krossing, *Angew. Chem.* **2007**, *119*, 5480–5484; *Angew. Chem. Int. Ed.* **2007**, *46*, 5384–5388. c) J. M. Slattery, A. Higelin, T. Bayer, I. Krossing, *Angew. Chem.* **2010**, *122*, 3297–3301; *Angew. Chem. Int. Ed.* **2010**, *49*, 3228–3231.
- [9] G. Bühler, C. Feldmann, Microwave-assisted Synthesis of Luminescent LaPO₄:Ce,Tb Nanocrystals in Ionic Liquids, *Angew. Chem. Int. Ed.* **2006**, *45*, 4864–4867. b) G. Bühler, D. Thölmann, C. Feldmann, One-pot Synthesis of Highly Conductive ITO Nanocrystals, *Adv. Mater.* **2007**, *19*, 2224–2227. c) M. Wolff, T. Harmening, R. Pöttgen, C. Feldmann, Sn₃I₈·2(18-crown-6) – a Mixed-valent Tin-Crown-Ether Complex, *Inorg. Chem.* **2009**, *48*, 3153–3156.
- [10] P. H. Svenson, L. Kloo, *Chem. Rev.* **2003**, *103*, 1649–1684.
- [11] a) A. J. Blake, R. O. Gould, S. Parsons, C. Radek, M. Schroeder, *Angew. Chem.* **1995**, *34*, 2374–2376; *Angew. Chem. Int. Ed.* **1995**, *34*, 2374–2376. b) K. F. Tebbe, R. Buchem, *Angew. Chem.* **1997**, *36*, 1345–1346; *Angew. Chem. Int. Ed.* **1997**, *36*, 1345–1346. c) C. J. Horn, A. J. Blake, N. R. Champness, A. Garau, V. Lippolis, C. Wilson, M. Schroeder, *Chem. Commun.* **2003**, *3*, 312–313. d) I. Pantenburg, I. Mueller, K. F. Tebbe, *Z. anorg. allg. Chem.* **2005**, *631*, 654–658.
- [12] K. F. Tebbe, R. Buchem, *Europ. J. Inorg. Chem.* **2000**, *6*, 1275–1282.
- [13] S. Menon, M. V. Rajasekharan, *Inorg. Chem.* **1997**, *36*, 4983–4987.

- [14] a) K. O. Stromme, *Acta Chem. Scand.* **1959**, *13*, 2089–2100. b) K. N. Robertson, P. K. Bakshi, T. S. Cameron, O. Knop, *Z. anorg. allg. Chem.* **1997**, *623*, 104–114. c) C. W. Cunningham, G. R. Burns, V. McKee, *Inorg. Chim. Acta* **1990**, *167*, 135–137.
- [15] a) N. Bricklebank, P. J. Skabara, D. E. Hibbs, M. B. Hursthouse, K. M. A. Malik, *J. Chem. Soc. Dalton Trans.* **1999**, 3007–3013. b) M. C. Aragoni, M. Arca, F. A. Devillanova, M. B. Hursthouse, S. L. Huth, F. Isaia, V. Lippolis, A. Mancini, H. Ogilvie, *Inorg. Chem. Comm.* **2005**, *8*, 79–82.
- [16] M. C. Aragoni, M. Arca, F. A. Devillanova, F. Isaia, V. Lippolis, A. Mancini, L. Pala, A. M. Z. Slawin, J. D. Woollins, *Chem. Commun.* **2003**, 2226–2227.
- [17] J. Taraba, Z. Zak, *Inorg. Chem.* **2003**, *42*, 3591–3594.
- [18] a) A. A. Tuinman, A. A. Gakh, R. J. Hinde, R. N. Compton, *J. Am. Chem. Soc.* **1999**, *121*, 8397–8398. b) B. Braida, P. C. Hiberty, *J. Am. Chem. Soc.* **2004**, *126*, 14890–14898. c) S. Riedel, T. Köchner, X. Wang, L. Andrews, *Inorg. Chem.* **2010**, *49*, 7156–7164.
- [19] a) V. A. Ozeryanskii, A. F. Pozharskii, A. J. Bienko, W. Sawka-Dobrowolska, L. Sobczyk, *J. Phys. Chem.* **2005**, *109*, 1637–1642. b) A. D. Tol, A. D. Natu, V. G. Puranik, *Mol. Cryst. Liq. Cryst.* **2007**, *469*, 69–77. c) H. Terao, T. M. Gesing, H. Ishihara, Y. Furukawa, B. T. Gowda, *Acta Cryst. E.* **2008**, *65*, m323.
- [20] a) A. Okrut, C. Feldmann, $\{[P(o\text{-tolyl})_3]Br\}_2[Cu_2Br_6](Br_2)$ - An Ionic Compound Containing Molecular Bromine, *Inorg. Chem.* **2008**, *47*, 3084–3087. b) D. Schneider, O. Schuster, H. Schmidbaur, *Dalton Trans.* **2005**, 1940–1947. c) S. Hauge, K. Marøy, *Acta Chem. Scand.* **1996**, *50*, 399–404. d) S. L. Lawton, R. A. Jacobson, *Inorg. Chem.* **1971**, *10*, 709–712.
- [21] M. Berkei, J. F. Bickley, B. T. Heaton, A. Steiner, *Chem. Commun.* **2002**, 2180–2181.
- [22] a) L. F. Vega, O. Vilaseca, F. Llovel, J. S. Andreu, *Fluid Phase Equilib.* **2010**, *294*, 15–30. b) J. Kumelan, D. Tuma, G. Maurer, *Fluid Phase Equilib.* **2009**, *275*, 132–144.
- [23] Ozin, G.; Arsenault, A. *Nanochemistry: A Chemistry Approach to Nanomaterials*; RSC Publishing: Cambridge, 2005.
- [24] Nedeljkovic, J. M.; Micic, O. I.; Ahrenkiel, S. P.; Miedaner, A.; Nozik, A. J. *J. Am. Chem. Soc.* **2004**, *126*, 2632.
- [25] Kan, S. H.; Aharoni, A.; Mokari, T.; Banin, U. *Faraday discussions* **2004**, *125*, 23.
- [26] Guzelian, A. A.; Katari, J. E. B.; Kadavanich, A. V.; Banin, U.; Hamad, K.; Juban, E.; Alivisatos, A. P.; Wolters, R. H.; Arnold, C. C.; Heath, J. R. *J. Phys. Chem.* **1996**, *100*, 7212.
- [27] Henkes, A. E.; Schaak, R. E. *Chem. Mater.* **2007**, *19*, 4234.
- [28] Eustis, S.; El-Sayed, M. *Chem. Soc. Rev.* **2006**, *35*, 209.
- [29] Wu, F. Y.; Yang, C. C.; Wu, C. M.; Wang, C. W.; Li, W. H. *J. Appl. Phys.* **2007**, *101*, 09G111.
- [30] Henley, S. J.; Carey, J. D.; Silva, S. R. P. *Appl. Surface Sci.* **2007**, *253*, 8080.
- [31] Kar, S.; Santra, S.; Chaudhuri, S. *Crystal Growth Design* **2008**, *8*, 344.
- [32] Soulantica, K.; Maisonnat, A.; Fromen, M. C.; Casanova, M. J.; Lecante, P.; Chaudret, B. *Angew. Chem. Int. Ed.* **2001**, *40*, 448.
- [33] Jeong, U.; Wang, Y.; Ibisate, M.; Xia, Y. *Adv. Funct. Mater.* **2005**, *15*, 1907.
- [34] Singh, P.; Kumar, S.; Katyal, A.; Kalra, R.; Chandra, R. *Mater. Lett.* **2008**, *62*, 4164.
- [35] Zhao, Z.; Zhang, Z.; Dang, H. *J. Phys. Chem. B* **2003**, *107*, 7574.
- [36] Khanna, P. K.; Jun, K. W.; Hong, K. B.; Baeg, J. O.; Chikate, R. C.; Das, B. K. *Mater. Lett.* **2005**, *59*, 1032.
- [37] Tsai, K. L.; Dye, J. L. *J. Am. Chem. Soc.* **1991**, *113*, 1650.
- [38] Chou, N. H.; Ke, X.; Schiffer, P.; Schaak, R. E. *J. Am. Chem. Soc.* **2008**, *130*, 8140.
- [39] Toneguzzo, P.; Viau, G.; Acher, O.; Guillet, F.; Bruneton, E.; Fievet-Vincent, F.; Fievet F. J. *Mater. Sci.* **2000**, *35*, 3767.
- [40] Xia, Y.; Xiong, Y.; Lim, B.; Skrabalak, S. E. *Angew. Chem. Int. Ed.* **2009**, *48*, 60.

- [41] Feldmann, C.; Jungk, H. O., Polyol-mediated Preparation of nanoscale Oxide Particles, *Angew. Chem. Int. Ed.* **2001**, *40*, 359.
- [42] Tuval, T.; Gedanken, A. *Nanotechnol.* **2007**, *18* 255601.
- [43] Hollemann, A. F.; Wiberg, N. Lehrbuch der Anorganischen Chemie, de Gruyter:, Berlin, 2007, p. 1182.
- [44] Mayya, K. S.; Caruso, F. *Langmuir* **2005**, *15*, 267.
- [45] Park, J.; Joo, J.; Kwon, S. G.; Jang, Y.; Hyeon, T. *Angew. Chem. Int. Ed.* **2007**, *46*, 4630.
- [46] Swanson, F. *Natl. Bur. Stand.* **1954**, *539*, 12.
- [47] Feldmann C 2003, Polyol-mediated Synthesis of Nanoscale Functional Materials, *Adv. Funct. Mater.* **13** 101.
- [48] Feldmann C and Jungk H O, Polyol-mediated Preparation of nanoscale Oxide Particles, 2001 *Angew. Chem. Int. Ed.* **40** 359.
- [49] Meshcheryakov V F, Fetisov Y K, Stashkevich A A and Viau G 2008 *J. Appl. Phys.* **104** 063910/1.
- [50] Hammarberg E, Prodi-Schwab A and Feldmann C, Microwave-assisted Synthesis of In₂O₃:Sn (ITO) Nanocrystals in Polyol Media and Transparent, Conductive Layers thereof, 2008 *Thin Solid Films* **516** 7437.
- [51] Kerner R, Palchik O and Gedanken A 2001 *Chem. Mater.* **13** 1413.
- [52] Buchold D H M and Feldmann C, Microemulsion Approach to Non-agglomerated and Crystalline Nanomaterials, 2008 *Adv. Funct. Mater.* **18** 1002.
- [53] Feldmann C, Matschulo S and Ahlert S, Polyol-mediated Synthesis of Nanoscale Mg(OH)₂ and MgO, 2007 *J. Mater. Sci.* **42** 7076.
- [54] Feldmann C, Preparation and Characterisation of Nanoscale Vb-Metal Oxides M₂O₅ (M = V, Nb, Ta), 2004 *Z. anorg. allg. Chem.* **630** 2473.
- [55] McAlister A J 1984 *Bulletin Alloy Phase Diagrams* **5** 247.
- [56] Hansen L D and Hart R M 2004 *Thermochim. Acta* **417** 257.
- [57] Davis J L and Barteau M A 1990 *Surface Sci.* **235** 235.
- [58] Chen J T, Shin K, Leiston-Belanger J M, Zhang M and Russell T P 2006 *Adv. Funct. Mater.* **16** 1476.
- [59] Mousavipour S, Hosein P and Philip D 1996 *J. Phys. Chem.* **100** 3573.
- [60] P. Cucka, C. S. Barrett, *Acta Crystallogr. A* 1962, **15**, 865.
- [61] J. Weidlein, U. Müller, K. Dehnicke, *Schwingungsspektroskopie*, Thieme, Stuttgart 1988.
- [62] K. Oldenburg, A. Vogler, *J. Organomet. Chem.* 1996, **515**, 245.
- [63] H. Nikol, A. Vogler, *J. Am. Chem. Soc.* 1991, **113**, 8988.
- [64] J. C. Sharma, J. Gandhi, A. Sharma, N. Gupta, S. Bhardwaj, *Internat. J. Chem. Sci.* 2008, **6**, 509.
- [65] S. Eustis, M. A. El-Sayed, *J. Phys. Chem. B* 2006, **110**, 14014.
- [66] Y. Xia, Y. Xiong, B. Lim, S. E. Skrabalak, *Angew. Chem.* 2009, **121**, 62; *Angew. Chem. Int. Ed.* 2009, **48**, 60.
- [67] P. Toneguzzo, G. Viau, O. Acher, F. Guillet, E. Bruneton, F. Fievet-Vincent, F. Fievet, *J. Mater. Sci.* 2000, **35**, 3767.
- [68] Z. C. Orel, E. Matijevic, D. V. Goia, *J. Mater. Res.* 2003, **18**, 1017.
- [69] A. Gautam, G. P. Singh, S. Ram, *Synth. Met.* 2007, **157**, 5.
- [70] T. Tuval, A. Gedanken, *Nanotechnol.* 2007, **18**, 255601.
- [71] B. Wiley, T. Herricks, Y. Sun, Y. Xia, *Nano Lett.* 2004, **4**, 1733.
- [72] S. Sun, C. B. Murray, D. Weller, L. Folks, A. Moser, *Science* 2000, **287**, 1989.
- [73] U. Jeong, Y. Wang, M. Ibisate, Y. Xia, *Adv. Funct. Mater.* 2005, **15**, 1907.
- [74] D. Li, S. Komarneni, *J. Am. Ceram. Soc.* 2006, **89**, 1510.
- [75] Y. Wang, Y. Xia, *Nano Lett.* 2004, **4**, 2047.
- [76] R. E. Balsells, A. R. Frasca, *Tetrahed.* 1982, **38**, 245.

- [77] B. L. Cushing, V. L. Kolesnichenko, C. J. O'Connor, *Chem. Rev.* 2004, **104**, 3893.
- [78] T. Oldag, H. L. Keller, *Z. Anorg. Allg. Chem.* 2004, **630**, 33.
- [79] C. Feldmann, $\text{CuBi}_7\text{I}_{19}(\text{C}_4\text{H}_8\text{O}_3\text{H})_3(\text{C}_4\text{H}_8\text{O}_3\text{H}_2)$ - a novel complex Bismuth Iodide containing one-dimensional $[\text{CuBi}_5\text{I}_{19}]^{3-}$ Chains, *Inorg. Chem.* 2001, **40**, 818.
- [80] S. Diewald, Y. Lan, R. Clérac, A. K. Powell, C. Feldmann, Drei Heterocubanartige ($\text{M}^{\text{II}}_4\text{O}_4$)-Typ Verbindungen ($\text{M} = \text{Fe}^{\text{II}}, \text{Co}^{\text{II}}, \text{Ni}^{\text{II}}$), *Z. anorg. allg. Chem.* 2008, **634**, 1880.
- [81] T. He, J. Yao, *J. Mater. Chem.* 2007, **17**, 4547.
- [82] T. Yamase, *Chem. Rev.* 1998, **98**, 307.
- [83] K. Matsubara, T. Tatsuma, *Adv. Mater.* 2007, **19**, 2802.
- [84] Y. Ohko, T. Tatsuma, T. Fujii, K. Naoi, C. Niwa, Y. Kubota, A. Fujishima, *Nature Mater.* 2003, **2**, 29.
- [85] D. L. Dorset, *J. Chem. Crystallogr.*, 1994, **24**, 219.
- [86] H. R. Oswald and W. Feitknecht, *Helv. Chim. Acta*, 1964, **35**, 272.
- [87] D. A. Scott, *Stud. Conservation*, 2000, **45**, 39.
- [88] S. C. Lee, S. H. Park, S. M. Lee, J. B. Lee and H. J. Kim, *Catalysis Today*, 2007, **120**, 358.
- [89] L. X. Yang, Y. J. Zhu, H. Tong, L. Li and L. Zhang, *Mater. Chem. Phys.*, 2008, **112**, 442.
- [90] Z. Chen and L. Gao, *Chem. Lett.*, 2008, **37**, 776.
- [91] C. L. Zhu, C. N. Chen, L. Y. Hao, Y. Hu and Z. Y. Chen, *J. Cryst. Growth*, 2004, **263**, 473.
- [92] H. Niu, Q. Yang and K. Tang, *Mater. Sci. Engeneer. B*, 2006, **135**, 172.
- [93] C. Feldmann, Polyol-mediated Synthesis of Nanoscale Functional Materials, *Adv. Funct. Mater.*, 2003, **13**, 101.
- [94] C. Feldmann and H. O. Jungk, Polyol-mediated Preparation of nanoscale Oxide Particles, *Angew. Chem. Int. Ed.*, 2001, **40**, 359.
- [95] L. B. Valdes, *Proceedings IRE*, 1952, **40**, 445.
- [96] V. K. LaMer, R. H. Dinegar, *J. Am. Chem. Soc.*, 1950, **72**, 4847.
- [97] P. Toneguzzo, G. Viau, O. Acher, F. Guillet, E. Bruneton, F. Fievet-Vincent, F. Fievet, *J. Mater. Sci.*, 2000, **35**, 3767.
- [98] H. Effenberger, *Acta Crystallogr.*, A 1950, **3**, 472.
- [99] J. Weidlein, U. Müller and K. Dehnicke, *Schwingungsspektroskopie*, Thieme, Stuttgart 1988.
- [100] T. Cseri, S. Bekassy, G. Kenessey, G. Liptay and F. Figueras, *Thermochim. Acta* 1996, **288**, 137.
- [101] R. A Street, W. S. Wong, S. E. Ready, M. L. Chabiny, A. C. Arias, S. Limb, A. Salleo and R. Lujan, *Mater. Today*, 2006, **9**, 32.
- [102] D. H. Lee, Y. J. Chang, G. S. Herman and C. H. Chang, *Adv. Mater.*, 2007, **19**, 843.